Dynamic Excitations in Membranes Induced by Optical Tweezers

Roy Bar-Ziv,* Elisha Moses,* and Philip Nelson#
*Physics of Complex Systems, Weizmann Institute of Science, Rehovot 76100, Israel, and #Department of Physics and Astronomy, University of Pennsylvania, Philadelphia, Pennsylvania 19104 USA

ABSTRACT We present the phenomenology of transformations in lipid bilayers that are excited by laser tweezers. A variety of dynamic instabilities and shape transformations are observed, including the pearling instability, expulsion of vesicles, and more exotic ones, such as the formation of passages. Our physical picture of the laser-membrane interaction is based on the generation of tension in the bilayer and loss of surface area. Although tension is the origin of the pearling instability, it does not suffice to explain expulsion of vesicles, where we observe opening of giant pores and creeping motion of bilayers. We present a quantitative theoretical framework to understand most of the observed phenomenology. The main hypothesis is that lipid is pulled into the optical trap by the familiar dielectric effect, is disrupted, and finally is repackaged into an optically unresolvable suspension of colloidal particles. This suspension, in turn, can produce osmotic pressure and depletion forces, driving the observed transformations.

1. INTRODUCTION

The function of biomembranes as tough, flexible partitions of cellular organelles involves a rich diversity of dynamic phenomena. Processes involving membrane shape transformations such as exocytosis are controlled by the specific action of molecular machinery, which transduces readily available chemical energy and uses it to overcome viscous damping and elastic energy barriers (Alberts et al., 1989). On the micron scale, cell membranes typically inhabit an environment out of equilibrium. Their motion is governed by the interplay between thermal energy, strong dissipation due to the surrounding fluid, and chemical energy. The thermal part is not only responsible for the incessant fluctuations of bilayers, but also leads to nontrivial entropic forces (Helfrich and Servuss, 1984; Evans and Rawicz, 1990). From a physical point of view, it is of interest to come up with simplified artificial membrane systems that can function as "micromachines" in a thermal environment. Can a system with no biological components exhibit dynamic processes similar to those occurring in the biological realm? We present here such a construction, composed only of lipid and water, with laser tweezers as the energy source.

Artificial membrane vesicles made of lipids ("liposomes") have been used extensively as model systems to study the physical properties of lipid bilayers. These include elasticity, equilibrium shapes and shape transitions, fluctuations, and adhesion (Deuling and Helfrich, 1976; Lipowsky and Sackmann, 1995; Lipowsky, 1991; Seifert, 1997). It is now widely recognized that most of the equilibrium properties of bilayers, on length scales much larger than the bilayer thickness, can be explained within the framework of the curvature elasticity model (Canham, 1970; Helfrich, 1973; Evans, 1974). This includes studies that have focused on relaxation dynamics in thermal equilibrium (Brochard and Lennon, 1975; Schneider et al., 1984; Döbereiner et al., 1995). Dynamic excitations of bilayers that take the membrane *out of equilibrium* have been less well studied, mainly because of the experimental difficulty in producing controlled perturbations in bilayers.

Our approach follows the spirit of the micropipette aspiration technique, which allows one to apply small forces on the membrane and measure the elastic response (Evans and Needham, 1987; Evans and Rawicz, 1990; Elbaum et al., 1996). Laser tweezers have added a new tool for applying weak forces (Ashkin, 1970, 1980; Ashkin et al., 1987; Svoboda and Block, 1994; Simmons et al., 1996). To date the technique has mainly been used to manipulate micron-size particles and to measure forces acting in macromolecular function (Ashkin, 1997). The novelty of applying laser tweezers to lipid bilayers lies not in the ability to drag objects, but rather in the variety of remarkable qualitative transformations that they create in membrane structures. In addition, laser tweezers offer excellent spatial and temporal resolution not available with other techniques.

When trapping macroscopic three-dimensional objects such as microbeads, one is concerned with the force applied by the tweezers. In contrast, when tweezers are applied to a two-dimensional surface we are interested in the energy transmitted per unit *area*, or in other words in the *surface tension* created by the laser. Laser-induced tension is one of the main ingredients of the theoretical picture to be elaborated below. Its existence is immediately clear when we tweeze a unilamellar giant floppy vesicle at a point along its contour. Within seconds of tweezing, the vesicle loses some of its area and becomes spherical with no visible fluctuations, a clear sign of tension (Bar-Ziv et al., 1995a).

Laser-induced tension proved to be the key to understanding our first new instability, the "pearling" transition

Received for publication 15 September 1997 and in final form 20 March 1998.

Address reprint requests to Dr. Roy Bar-Ziv, Center for Physics and Biology, Rockefeller University, 1230 York Ave., New York, NY 10021. Tel.: 212-327-8160; Fax: 212-327-7406; E-mail: barzivr@rockvax.rockefeller.edu.

0006-3495/98/07/294/27 $2.00

(Bar-Ziv and Moses, 1994; Nelson et al., 1995). Long cylindrical vesicles subject to laser tweezing at a point undergo a dramatic shape transformation into a modulated structure of a string of pearls completely delocalized from the tweezing point. The origin of this instability is a competition between the induced tension and the bending elasticity of the bilayer, as we have shown; we have quantified and characterized it, yielding a satisfactory agreement between experiment and theory (Goldstein et al., 1996; Bar-Ziv et al., 1997b).

However, when examining the response of complex vesicular structures in which small vesicles are encapsulated within larger ones, it becomes apparent that tension cannot be the only ingredient in the physical picture of the laser-membrane interaction. When a parent vesicle has become round by laser tweezing, it can then expel an encapsulated daughter vesicle, either spontaneously after the laser is shut off, or by continuous tweezing. We will argue below that two new concepts are required to explain the observations: osmotic flow (Moroz et al., 1997) and a new "colloidal creeping" mechanism to be introduced below. Both of these mechanisms are rooted in the observation of irreversible loss of membrane under the laser action. We will propose a picture in which the area detached from the bilayer by the laser is repackaged in the form of a suspension of small particles (membrane fragments) that can produce osmotic effects and depletion forces similar to those observed in other colloidal systems.

Several of the phenomena described in this paper were announced in earlier publications (Bar-Ziv and Moses, 1994; Nelson et al., 1995; Bar-Ziv et al., 1995a,b, 1997b; Goldstein et al., 1996; Moroz et al., 1997). The purpose of this paper is to bring these results together, to describe new results not previously described, and to create a unified physical picture capable of explaining most of them. The organization of the paper is as follows. In Section 2 we present our physical picture for the interaction of the focused laser beam that forms the optical tweezers with a fluid lipid bilayer. Section 3 is devoted to experimental procedures, protocol, and data analysis methods. In Section 4 we review the pearling instability, which is currently our best studied laser-induced dynamical shape transformation, and in Section 5 we present new results on expulsion in closed vesicles. In Section 6 we present excitations of bilayers in planar structures, where the laser induces local unbinding and can create topological excitations. Finally, we present new results on exotic excitations of vesicles with a high surface-to-volume ratio.

2. PHYSICAL PICTURE

In this section we will sketch a unified physical picture of the interaction of laser tweezers with a lipid bilayer, then review the qualitative experimental evidence for the specific elements of this picture. In the sequel we will then use the picture to understand, in some cases quantitatively, several of the most striking membrane transformations.

2.1. Laser-induced tension

The heart of the experiment is a $\lambda = 514$ nm argon laser and an optical microscope with a strongly focusing objective lens. Giant vesicles of various sizes and shapes are prepared by swelling pure lipids (typically dimyristoylphosphatidylcholine (DMPC)) in water. The optical trap is produced by focusing up to $I = 50$ mW of laser intensity from a beam 6 mm in diameter into a spot of size $w_0 \approx 0.3$ μm (Svoboda and Block, 1994; Simmons et al., 1996). A strong gradient of light intensity is set at the focus of the objective lens, and a huge power density, 20 MW/cm^2, passes through the $D =$ 4-nm-thick bilayers under study. Most of this energy just passes through with minimal absorption and heating, because the membrane is a thin transparent material at the laser wavelength (see below). However, a tiny amount of electromagnetic energy, U, does interact with the lipid and goes into polarizing it. This is

$$U = (\epsilon_L - \epsilon_W) \int \langle |E|^2 \rangle dV, \tag{1}$$

where ϵ_L and ϵ_W are the dielectric constants of the lipids and water in the visible range, and $\langle |E|^2 \rangle$ is the time-averaged electric field intensity. The integral extends over the volume of interaction of the electromagnetic field with the membrane. Because the thickness of the membrane D is much smaller than its lateral size, we can transform the integral into a surface integral over the area of the membrane in the trap. Using $\langle |E|^2 \rangle = I/w_0^2$, where c_W is the speed of light in water, we get

$$U = \Sigma_L \int_{S_t} dS, \tag{2}$$

where

$$\Sigma_L \equiv \frac{(\epsilon_L - \epsilon_W) ID}{c_W w_0^2} \approx 4.5 \cdot 10^{-5} \text{erg cm}^{-2}/\text{mW} \cdot I. \tag{3}$$

Because of the strong focusing of the Gaussian beam, the integral extends over an area of $S_t \approx w_0^2$, which is much smaller than the total area of the vesicle. Σ_L is an *upper limit* on the tension that could be induced in the membrane. In practice the actual tension will reflect only the *net* energy gain σ after the membrane has been folded to fit into the trap (see Section 2.4 below). For laser intensity $I = 10$ mW, $\Sigma_L \approx 5 \times 10^{-4}$ erg/cm^2. As we will see, this is comparable to the tension needed to induce shape transformations in micron-size membrane structures. The corresponding interaction energy is $U \approx 10^{-12}$ erg, comparable to the bending rigidity of the bilayer and not much more than the thermal energy $k_B T$. It is important to note that because of the diffraction limit, $w_0 \propto \lambda$. Therefore, the laser-induced tension drops significantly with wavelength,

$$\Sigma_L \propto 1/\lambda^2, \tag{4}$$

favoring in this case the use of an argon laser over near IR lasers, such as the commonly used 1064 nm YAG laser.

2.2. Membrane elasticity and entropic tension

What is the response of a lipid membrane to a local tension of 10^{-4}–10^{-3} erg/cm^2? To answer this question we must recall some elements of membrane elasticity (for a recent textbook see Safran, 1994). Lipid molecules self-assemble strongly into bilayer membranes. Any deformation of the membrane that changes the packing of molecules from their optimum arrangement will incur an elastic free-energy cost, but some deformations are far less costly than others. For example, bending a bilayer deforms its individual monolayers, but by a small amount proportional to D/ℓ, where D is the membrane thickness and ℓ is the radius of curvature. Indeed, bends on the micron scale are so much easier than net stretching of the membrane that we may neglect the latter completely. This will be true as long as the applied tension Σ remains much less than the intrinsic stretch modulus of the membrane, which is the scale of interest to us. The free energy cost of a membrane configuration is then given by

$$E = \frac{\kappa}{2}\int\left(\frac{1}{R_1}+\frac{1}{R_2}\right)^2 \mathrm{d}S, \tag{5}$$

where $\kappa \approx 10 - 15\ k_BT$ is the bending rigidity, R_1 and R_2 are the principal local radii of curvature, and the integral is over the surface of the membrane, the total area of which is fixed.

At zero temperature an ideal unconstrained membrane will adopt its preferred surface density of lipid molecules and thus attain zero tension. At finite temperature thermal fluctuations soften the membrane and effectively render it stretchy: a weak external force acting on the membrane can unfold thermal wrinkles, increasing its apparent area without actually changing the microscopic surface density of molecules in the bilayer. Conversely, constraining the thermal fluctuations in a membrane lowers the entropy and generates a free energy cost per unit area or, in other words, an effective tension. For example, fluctuations can be constrained by the combined constraints of fixed number of lipid molecules and fixed enclosed volume. Thus a closed vesicle will always have some nonzero surface tension. This has been established theoretically and beautifully demonstrated experimentally by Evans and co-workers (Helfrich and Servuss, 1984; Milner and Safran, 1987; Evans and Rawicz, 1990; Seifert, 1995a). For 10-μm-size lipid vesicles, under no applied force, tension values are as low as 10^{-6} erg/cm^2. In fact, this "entropic elasticity" persists over five orders of magnitude, up to 0.1 erg/cm^2, before the bilayer becomes a normal linearly elastic material (Evans and Rawicz, 1990). We dwell on this point because the optical tweezers (somewhat fortuitously) operate in the middle of this entropic regime.

Thus optical tweezers turned out to be a suitable tool for exciting dynamic shape transitions in bilayers, essentially because of the clear separation of energy scales between the soft, low-energy bending modes of the membranes and the highly energetic stretching modes. Laser-induced tension of 10^{-3} erg/cm^2 is a weak tension excitation compared with the stretching modulus of $\sim$100 erg/cm^2, but high when compared with the equilibrium tension of $\sim 10^{-6}$ erg/cm^2.

2.3. Dynamics of tension and shape transformations

Because the membrane is a two-dimensional fluid, we should think of its surface tension as a negative 2D pressure. What we have argued, then, is that the effect of the laser is to maintain this pressure at some value Σ just outside the trap. What happens next depends crucially on the initial membrane configuration.

Tweezing an infinite planar membrane, or a very large flaccid vesicle, will simply result in a slow inflow of material to the trap. The flow will be impeded by the viscous loss of the water it entrains (plus a negligible loss from the thin bilayer itself), so that the tension in the membrane becomes negligible outside a radius a few times the trap size. Indeed, when tweezing in this configuration, we do observe free Brownian fluctuation of the membrane away from the trap.

More interesting phenomena can happen in other configurations. As mentioned earlier, a spherical vesicle has minimized its projected area for the given enclosed volume, and is under tension. Applying additional tension cannot further decrease its surface area without releasing volume. In this case material flows into the trap until the tension is equal to Σ everywhere. If the laser is turned off at this point, then this equilibrium will be maintained. We will see below how this tense state can store enough energy to drive membrane reorganization. Perhaps most interesting, however, is the case of an initially *cylindrical* vesicle of radius R_0. Like the sphere, a cylinder cannot lose any surface area at fixed volume without changing to some other shape. Plateau (1873) studied this problem in the previous century and noted that a small periodic perturbation in the cylindrical shape could reduce area at fixed volume if its wavelength exceeded $2\pi R_0$. Indeed, we have not seen an initial disturbance of wavelength shorter than this.

Moreover, because of the volume constraint, the area loss (and hence the energy gain due to the work done by the laser) is proportional to the square of the perturbation amplitude. Because the cylinder was initially a metastable equilibrium shape, any shape perturbation costs some elastic bending energy, again proportional to the square of the amplitude. (In contrast, a flaccid vesicle reduces its bending energy by becoming more spherical.) Thus we get a competition: no shape change occurs unless Σ exceeds a critical value $\Sigma_{\mathrm{pearl}} \sim \kappa/R_0^2$ (Bar-Ziv and Moses, 1994; Nelson et al., 1995; Goldstein et al., 1996). Before the tension reaches

this value, the cylinder is *effectively rigid*; tension must therefore spread out through the incompressible membrane (as in the spherical case) instead of being lost to viscous drag as the vesicle shape rearranges locally (as in the flaccid vesicle case).

Indeed, this situation persists even after Σ rises past the pearling threshold (Goldstein et al., 1996). Here again the key is the confined geometry of a thin cylinder. The fluid volume which must rearrange for a shape change scales linearly with the amplitude $(u)t$ of the modulation, and so the rate of viscous energy loss is proportional to the viscosity η of water and to $\dot{u}^2$. On the other hand, the energy gain from the laser scales as u^2 and so its rate is proportional to $\Sigma\dot{u}u$. Thus initially the modulation grows at a slow rate fixed by Σ/η. Dimensional analysis then suggests that it also moves at a velocity $v_f \sim \Sigma/\eta$, and indeed we found that this is an overestimate. Tension, on the other hand, spreads diffusively in a nearly incompressible membrane of nearly fixed shape. Here dimensional analysis suggests a diffusion constant of KR_0/η, where $K \approx 100$ erg/cm^2 is the bulk elastic modulus of the membrane.

Thus we find that tension initially outruns the advancing shape transformation. Although constant-velocity propagation eventually catches up to diffusive spread, it turns out that K is large enough that this does not occur in the observable region of the initial pearling propagation (Goldstein et al., 1996); we may thus take tension to be a constant equal to Σ throughout the pearling instability.

2.4. Detachment and escape of lipids

When a lipid molecule enters the laser spot, displacing water, the system gains electric energy via Eq. 1. We found that continuous tweezing results in an irreversible loss of membrane surface area: for example, vesicles made round and tense by the laser action remain that way indefinitely. Over 100 μm^2 of membrane can disappear in this way. Thus, even though we cannot optically resolve the details of this process, we can nevertheless infer that lipids detach and escape from the membrane. Usually the remaining membrane does not become darker, and blobs of bulk lipid do not form, so some of the lost material must form membrane fragments of a size well below our ~200-nm resolution. Moreover, the trap volume of $\sim 3 \times 10^{-14}$ cm^3 is too small to contain all of the lost lipid, up to 100 μm$^2 \times 4$ nm.

We gain further evidence that lipid is not simply folding up inside the laser trap when we note that packing extra material into the spot would require bending the membrane, incurring a curvature energy penalty. If we assume that the membrane bends with a wavelength characterized by the trap size, we get a lower bound for the packing cost per unit area: $\Sigma_c \gtrsim 4\kappa/w_0^2 \approx 3 \times 10^{-3}$ erg/cm^2. Only for $\Sigma_L > \Sigma_c$ would the membrane gain net energy proportional to $\Sigma \equiv \Sigma_L - \Sigma_c$ by entering the trap. Experimentally we observe a threshold for tension effects at laser intensities of $I_c \approx 1$–10 mW, which corresponds to $\Sigma_c \approx 0.5$–5×10^{-4} erg/cm^2. Either our estimate for Σ_c is too high, or we must deduce that the huge energy flux through the bilayer creates additional effects that supply the energy needed to repackage the lipids. (One could suppose that self-adhesion effects inside the trap reduce Σ_c somewhat, but the required near-cancellation of the folding energy seems unlikely to us.)

We propose that the lipid is pulled inside the trap and then pinched off the vesicle as little membrane fragments, as shown in Fig. 1. We do not have a microscopic model for this process; although we argue below against global heating, we cannot rule out a local radiation effect on the lipids inside the trap, a fact that might cause fragmentation and assist lipid loss from the membrane.

Once formed, small fragments can easily escape the trap, making room for more membrane to enter. To understand why large, organized lipid structures like membranes are pulled into the trap, whereas small fragments escape, we recall that many small objects have much more *entropy* than a few large ones. Put differently, every fragment has thermal energy $3k_BT/2$ regardless of size, whereas its confining energy well due to the dielectric effect is proportional to its total number of lipid molecules. Thus whereas small fragments are disfavored because of their large curvature energy, only large fragments can remain trapped in the laser spot by the dielectric effect; the escaping fragments will be dominated by those smaller than

$$r_{\text{colloid}} \lesssim \left(\frac{3k_BT}{8\pi\Sigma_L}\right)^{1/2}.$$

For typical laser intensities we find that $r_{\text{colloid}} \lesssim 20$ nm, indeed below our 200-nm resolution. *For illustration* we will make below the perhaps optimistic estimate that the fragments are 5 nm in radius, a typical size for micelles, although the lipids in question do not spontaneously form micelles (Marsh, 1990). Vesicle suspensions nearly this small can readily be created by extrusion or sonication and are long-lived (Goll and Stock, 1977; Goll et al., 1982).

We argue in Section 5.2.3 that this irreversible loss of membrane into solution and the subsequent colloid of small

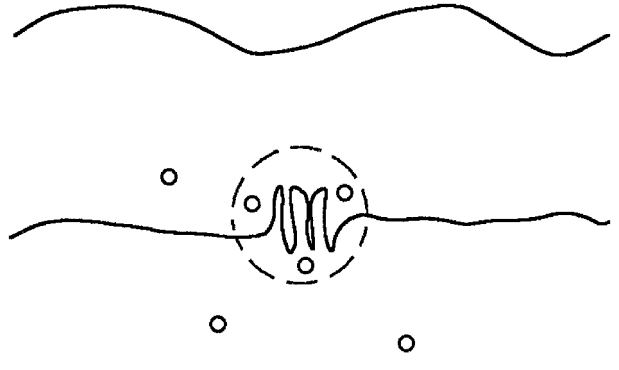

FIGURE 1 A cartoon of the effect of laser tweezers on a lipid bilayer. Lipid is packed into the laser spot by buckling and bending of the bilayer inside the laser spot. Eventually lipid fragments detach and escape the trap.

particles thus formed in closed vesicles furnish the driving force for laser-induced spontaneous expulsion.

2.5. Colloidal effects

In the previous subsection we argued that the laser could create a colloidal suspension of small membrane fragments. Any such particles created outside a confined region will simply diffuse away, whereas those created inside a vesicle remain trapped and can lead to a number of surprising effects.

As long as the vesicle wall retains its integrity, any osmotic activity of membrane fragments will be negligible because of the far greater number of unavoidable small solute particles. The latter will clamp the vesicle volume because of their extremely slow diffusion through bilayer membranes (Alberts et al., 1989). Thus, for example, we expect no colloidal effect in the case or pearling: here there is very little area loss, the tweezing times can be quite small (under a second), and there is no membrane gap to permit osmotic flow.

Suppose, however, that a hole opens in the membrane, of a size intermediate between small solutes (like sugar) and r_{colloid}. Then small solutes will exchange freely, leaving only the osmotic effect of the membrane fragments. Because the large fragments are concentrated inside, the net effect is to *pull water into the vesicle*, and thus create an interior pressure. In Moroz et al. (1997) we argued that this effect supplies the driving force for vesicle expulsion.

Another well-known colloidal effect is the "depletion interaction" (Israelachvili, 1991). Normally one thinks of two rigid surfaces in a colloidal suspension. Each surface of area A is surrounded by a small "depletion volume" Ar_{colloid}: the center of each colloidal particle must stay outside this volume. The entropic cost of this forbidden volume can be eliminated by bringing the two surfaces into contact, eliminating depletion volume and leading to a free energy gain. Equivalently, we can imagine the two surfaces being held together by an effective *suction*, given by the osmotic formula $p_{\text{eff}} = -3k_{\text{B}}T\phi/4\pi(r_{\text{colloid}})^3$, where ϕ is the volume fraction. We get an upper bound on this pressure by taking $r_{\text{colloid}} \approx 5$ nm, the size of micelles, and $\phi \approx 0.3$. Then $-p_{\text{eff}} \lesssim 2 \times 10^4$ erg/cm^3, a sizable pressure indeed.

We will see in Section 5.2.3 that inside a large vesicle, the expected volume fraction is actually many thousands of times smaller than unity, because the laser destroys only a limited amount of membrane. However, in more confined spaces, such as the thin layer between two bound bilayers, ϕ can indeed approach unity, leading to large effects. Suppose, for example, that a bilayer edge is in contact with a second bilayer, as occurs during vesicle expulsion. The sliding contact keeps a $\phi \approx 1$ suspension on one side separated from pure water on the other. In this situation the sliding edge will feel an entropic force pushing it toward the colloid side, because motion in this direction reduces the area exposed to the colloid and hence the entropically costly depletion volume, with no corresponding increase on the pure water side. We call this effect "colloidal creeping."

The free-energy gain from colloidal creeping can also be considerable: multiplying p_{eff} by r_{colloid} in the above example gives an upper bound of 0.01 erg/cm^2, again in the range of interest to us and, as we will see in Section 5.3.2, sufficient to enlarge a membrane pore once it forms.

2.6. Experimental evidence for the physical picture

Before giving our detailed procedures and observations, we will give some qualitative facts and simple estimates supporting the general physical picture sketched in the previous subsections.

First we verify that the laser can apply forces of the expected magnitude. Fig. 2 shows the result of pulling a very large flaccid vesicle. We show a section, ~80 μm long, of a much larger giant digalactosyldiglyceride (DGDG) vesicle. Tweezing at a point (*arrow* in Fig. 2, *b–d*) we were able to deform the membrane contour by slowly

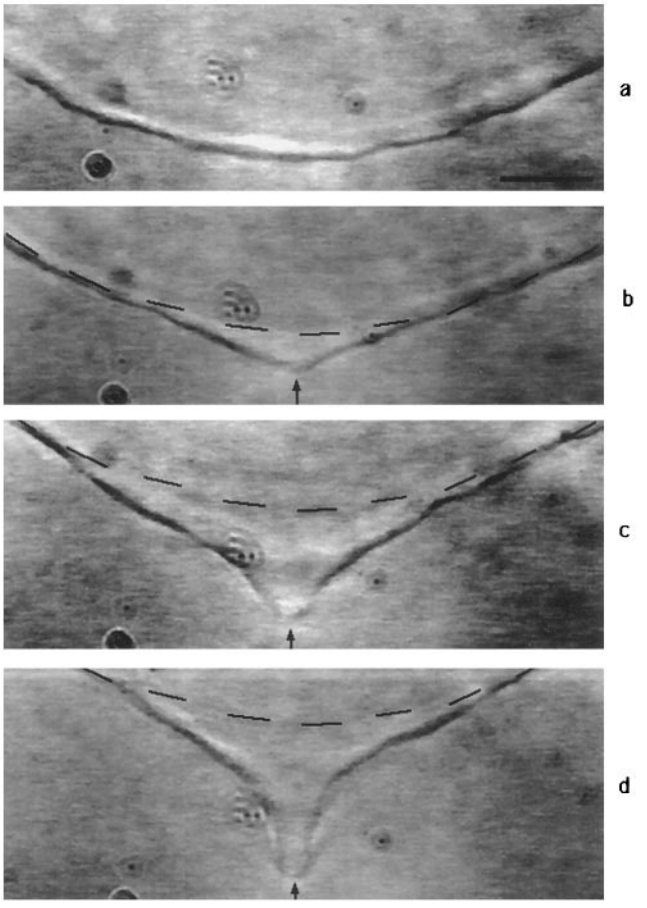

FIGURE 2 Mechanical manipulation of a membrane. The line is a two-dimensional section from a DGDG giant vesicle that spanned the whole of the sample cell and filled more than our video frame. The vesicle was observed after hours of swelling in the sample cell. The dashed line in *b–d* indicates the undeformed contour of *a*; the arrow defines the point of tweezing. The bar is 10 μm.

dragging it against the restoring elastic forces. Beyond a certain deformation (Fig. 2 *d*), the restoring force overcame the optical force and the membrane popped out of the trap, then slowly relaxed back to the thermal equilibrium contour of Fig. 2 *a*. Throughout the process, the vesicle continued to exhibit visible thermal fluctuations, indicating that the induced tension is negligible, as expected from our discussion in Section 2.3 above.

The maximum applied optical force can be estimated by measuring the deformed contour at mechanical equilibrium (Fig. 2 *d*). The contour in Fig. 2 *d* subtracted from that in Fig. 2 *a* was approximated by a best fit to a Lorentzian,

$$h(x, y) = \frac{h_0}{(x^2 + y^2)/a^2 + 1}, \tag{6}$$

with $h_0 = 16$ μm and $a = 3.4$ μm. We computed the elastic bending energy $E = \frac{1}{2}\kappa\int(\nabla^2 h)^2 \mathrm{d}S$, where $\kappa = 0.4 \times 10^{-12}$ erg is the bending modulus and dS is the surface element. Integrating over the surface deformation gives $E = 3 \times 10^{-11}$ erg. The optical force balancing the elastic restoring force is roughly $\partial E/\partial h_0 \approx 4 \times 10^{-8}$ dyn. The tension associated with such a force is ultralow, $\Sigma \approx F/h_0 \approx 2 \times 10^{-5}$ dyn/cm, comparable to the minimum value for a flaccid vesicle mentioned in Section 2.2 above.

We can further verify the magnitude of the optical force deduced from the mechanical pulling experiment by dragging a spherical vesicle with the tweezers. This is a standard procedure for calibrating maximum trapping forces on spherical beads (Svoboda and Block, 1994; Simmons et al., 1996). For a given trapping intensity there is a maximum dragging velocity V, above which the trapped vesicle will pop out of the trap. At that velocity the optical trapping force and the Stokes' drag force coincide. Typically we measure $F = 6\pi\eta RV \approx 10^{-8}$ dyn, or 0.1 pN. This result is at least an order of magnitude less than the trapping force measured on beads of similar size, because of the fact that the membrane is a two-dimensional object and hence the optical force is weaker.

Turning to the specific phenomena of interest to us, we mentioned in Section 2.3 that a cylindrical vesicle under sudden, uniform tension should have a threshold $\Sigma_{\mathrm{pearl}} \approx \kappa/R_0^2$, below which no shape transformation occurs. Indeed, we have observed that for a membrane tube of radius $R \approx 1$ μm made from DMPC lipid with a bending rigidity $\kappa \approx 10^{-12}$ erg, there is a threshold laser power for pearling that corresponds under Eq. 3 to $\Sigma_{\mathrm{pearl}} \approx 10^{-4}$ erg/cm^2, as expected, a direct confirmation for the energy scale of the laser-membrane interaction.

Tension alone cannot explain all of our phenomena, however. In the expulsion experiment the laser puts a vesicle of radius R under tension, but then is shut off. The vesicle then spontaneously opens a pore to allow the expulsion of an interior object of radius r. One might naively suppose that the surface tension pulls open the pore. But an $R = 4.5$ μm vesicle under a tension of 10^{-3} dyn/cm has an area only 1% greater than the same membrane under zero external tension (Seifert, 1995a). If the only energy storage mechanism were stretching of the membrane, all of the stored energy would be spent by the time a pore of a size 1% the total vesicle area had formed, or equivalently, by the time a volume 1.5% of the total vesicle volume had exited through this pore. Because the daughter object can have a volume up to 50% of the parent vesicle (see Section 5.2 below), some other mechanism must be forcing water into the space between the parent and daughter, pushing the daughter out. The only mechanism that can force water against a pressure gradient is osmosis, and yet initially the fluids inside and out were identical. In Section 5.2.3 we will argue that the colloid proposed in the previous subsection provides the required osmotic activity.

3. EXPERIMENTAL PROCEDURES

3.1. Setup

The optical tweezers were set up using an inverted microscope, a high numerical aperture lens, and an argon laser. The 488–514-nm Ar ion laser beam (Coherent, Innova 70) creates a tighter beam waist than infrared lasers, and therefore a stronger electromagnetic field. Fig. 3 is a schematic drawing of the setup. The inset is a close-up view of the vesicle suspension chamber with a temperature control system with excellent long-term stability of 5 mK.

The suspension of vesicles was kept in a closed sample cell made from two thin coverslips sealed by wax or epoxy with a 50-μm mylar spacer. The cell was in contact with the objective lens on the bottom, and from the top it was attached with immersion oil to a sapphire window that was the bottom plate of a temperature-controlled chamber. The temperature of the sapphire window and the objective lens was maintained by using water flowing in a closed loop from a commercial heater-refrigerator bath (Lauda). The objective lens was also encased in a copper thermal sleeve encircling it, through which water from the temperature-regulated bath flowed. In principle, the bath can stabilize temperature to within $\pm$0.01K, but because of heat losses we achieved only $\pm$0.1K. Fine regulation of the temperature within the vesicle cell was achieved by a thin foil heater (Minco) in the shape of an annulus placed between the sapphire and the vesicle cell. The temperature of the cell was monitored by a thermistor with a negative temperature coefficient and a sensitivity of $\sim$3000 Ω/K, which constituted one leg of a Wheatstone bridge balanced by a precision (0.01%) resistance decade. The signal was fed back through a differential integrator and amplifier to a voltage-controlled power amplifier heating the foil. (We are grateful to Y. Barad and V. Steinberg for providing us with their homemade low-noise instrumentation amplifier.) The temperature was set such that the heater always heated in steady state. Using an integration time of $\sim$10 s, the system averages out fluctuations and obtains long-term stability of 5 mK with $\sim$1 W heating the foil.

3.2. Materials and preparation

Vesicles were prepared from commercially available lipids (Sigma), DMPC, stearoyloleoylphosphatidylcholine (SOPC), and DGDG, all of them uncharged, zwitterionic lipids, by standard protocols (Evans and Needham, 1987), as described below. As far as we could tell, our results were not specific to one type of lipid, and all of the lipids we have used consistently displayed the same response to tweezing. In the following we shall not emphasize the chemical differences, because of the overall similarity in behavior. We preferred to work with lipids whose melting temperature was conveniently below our ambient working room temperature. Lipid powder was added to a mixture of methanol and chloroform (2:1) at a concentration of 10 mg/ml. To produce giant vesicles, we deposited $\sim$20 μl of lipid solution on a Teflon disk placed inside a beaker.

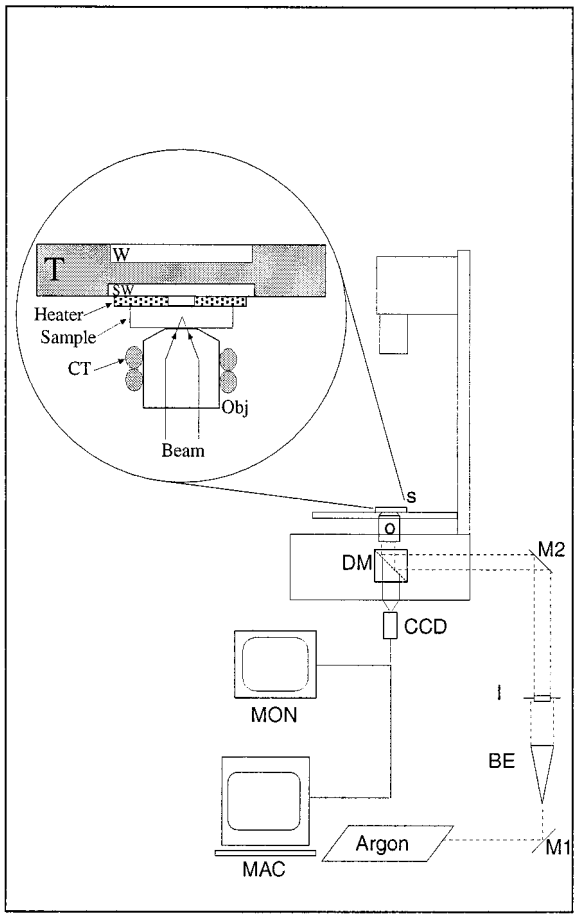

FIGURE 3 Argon: argon laser (Coherent Innova 70) operating in the 514.5 line. M1 and M2: mirrors. BE: beam expander composed of two positive lenses. I: iris diaphragm. Inverted microscope (Zeiss Axiovert 135). DM: dichroic mirror. CCD: CCD camera (Hamamatsu c2400 or Cohu 6500). MON: Monitor. O: microscope objective (Zeiss plan-apochromat Phase ×63/1.4). Images are taken into the computer (Macintosh, Quadra 800) using a frame grabber (Data Translation) and Image software (NIH). S: sample. Inset: Obj: Objective Lens. CT: Copper tubing. Heater: thin foil 50 Ω (Minco). SW: sapphire window. W: optical window. T: temperature-regulated stage.

The Teflon was thoroughly cleaned before being used and was roughened with emery paper, as described by Evans and Needham (1987). The methanol/chloroform solvent was allowed to evaporate and then was dried under vacuum. This assists in obtaining a higher yield of unilamellar vesicles. Then a few milliliters of pure water or 0.1–0.5 molar sugar solution, heated to 40°C, was added, and the beaker was left in the oven overnight at a temperature of 40°C. Vesicle suspensions were readily identified as typical "clouds" and were gently aspirated into a syringe, then transferred into the microscope cell. Glass components were cleaned by sonication in detergent and water, followed by multiple thorough rinses in ultrapure water (Barnstead E-pure). This was followed by sonication in an organic solvent, usually ethanol, for ~10 min. The experiments were performed in the fluid state of the membranes in a closed cell, typically at 15–20°C above the fluid-gel transition point.

A different preparation technique incorporating a simple kinetic procedure was used to produce long cylindrical structures. A few microliters of lipid solution was deposited on a clean coverslip and left for a few hours under vacuum in a desiccator, to allow the solvent to evaporate. Two slices of mylar, 50 μm thick, were placed on the glass as spacers, and an upper coverslip was fixed to the bottom one with epoxy or melted wax, leaving two opposite sides unglued. Warm water was then injected from the side into the cell with a syringe. This induced a flow capable of carrying along globules of lipids, which started to swell from the deposit on the bottom coverslip. This injection procedure could be repeated a few times to create a number of strong flow pulses in the cell. Within a few hours of swelling, we observed tubes oriented in the direction of the flow extending over hundreds of microns, typically anchored at both ends to lipid globules that were still attached to the bottom coverslip. These structures remained metastable for hours to days.

3.3. Image analysis

Quantitative image analysis was carried out to follow dynamic shape transformations of vesicles. We implemented a fast digitization algorithm of the two-dimensional contour extracted from the frame grabber, written as a user-defined interface within the NIH Image software. Döbereiner (1995) has presented excellent image analysis procedures to study vesicle shape transformations. A contour of a membrane obtained with phase-contrast microscopy is approximated by the contour perpendicular to the steepest gradient of intensity along the typical halo profile. By measuring the intensity distribution of the video pixels, one can locate the nominal line, to better than one-pixel resolution, using a smooth interpolating scheme (Döbereiner, 1995). This kind of analysis is somewhat time consuming, but is necessary for small shape changes.

In none of our shape changes did we need such an elaborate algorithm, and hence we developed a faster algorithm that finds the membrane contour to within pixel resolution, compromising for some digitization noise. The algorithm probes the vicinity of a contour point by averaging the pixel intensity over 13 pixels in eight directions and locating the contour point in the direction of maximum intensity, similar to the method of Duwe et al. (1990). Once a set of points $\{x_i, y_i\}$ is found, we smooth out the contour and can proceed to analyze the shape changes according to need, as described in the specific sections below.

Once the contour was determined, we could measure a number of quantities to follow the shape changes and the fluctuations. A simple way to follow the decrease in fluctuations during tweezing (Section 5.2.1) and adhesion deformation (Section 5.2.2) of spherical vesicles was to measure the fluctuations in the normalized mean square of the radius. These are defined as

$$\frac{\langle R^2\rangle - \langle R\rangle^2}{\langle R\rangle^2}, \tag{7}$$

where

$$\langle R\rangle = (1/N)\sum_{i}^{N} |\vec{R}_i(x,y) - \vec{R}_{CM}| \tag{8}$$

is the average radius of the contour relative to the center of mass, and similarly for $\langle R^2\rangle$.

To quantify the shape fluctuations of open contours (Section 5.3.2), we transform to the arclength parameterization:

$$s_i = s_{i-1} + \sqrt{(x_i - x_{i-1})^2 + (y_i - y_{i-1})^2} \tag{9}$$

$$\Psi_i = -\arctan\left(\frac{y_{i+1} - y_{i-1}}{x_{i+1} - x_{i-1}}\right), \tag{10}$$

with proper care taken at the boundaries. From the starting point, $s = 0$, to the end point, $s = s^*$, we computed the tangent angle to the contour, $\Psi(s)$. For each contour we numerically computed two parameters: the "curvature integral,"

$$\left\langle \left(\frac{d\Psi}{ds}\right)^2 \right\rangle \equiv \frac{1}{s^*}\int \left(\frac{d\Psi}{ds}\right)^2 ds, \tag{11}$$

and the "surface integral,"

$$\langle \Psi^2 \rangle \equiv \frac{1}{s^*} \int \Psi^2 ds. \tag{12}$$

These two quantities will help us evaluate and distinguish the geometric contributions to the energy of the membrane, arising either from changing the surface or from changes in the curvature.

Finally, to analyze the shape deformations in detail for axisymmetrical shapes (Section 5.3.3), we used the mode expansion method developed by Döbereiner (1995). For each frame we rotated and translated the contour so that it was aligned with the major axis of the inertia tensor. One can then parameterize the vesicle contour by the tangent angle to the contour arclength $\Psi(s)$ measured for each half-contour from the north pole, $s = 0$, to the south pole at $s = s^*$. Thus,

$$\Psi(s) = \pi \frac{s}{s^*} + A_1 \sin\left(\pi \frac{s}{s^*}\right) + A_2 \sin\left(2\pi \frac{s}{s^*}\right) + A_3 \sin\left(3\pi \frac{s}{s^*}\right) + \cdots \tag{13}$$

A_2 measures the ellipsoidal deformation of the sphere (Döbereiner, 1995):

$$A_2 = 1 + \sum_i \left(\Psi_i \sin\left(2\pi \frac{s_i}{s^*}\right) + \Psi_{i+1} \sin\left(2\pi \frac{s_{i+1}}{s^*}\right) \right) \frac{s_{i+1} - s_i}{s^*}. \tag{14}$$

3.4. Heating and absorption

Working with focused laser and biological materials, one is always concerned with radiation heating effects. The most direct evidence that there is no global heating of the water is that the membrane does not respond unless the laser is applied directly to it. To further confirm this, we measured the absorption directly and estimated the amount of heating due to absorption at the laser wavelength by assuming that the trap is a localized heat source (Block, 1990). The steady-state temperature rise of the surrounding liquid is $\Delta T = I_{abs}/\lambda R$ (Block, 1990), where I_{abs} is the intensity absorbed at the laser wavelength, λ is the thermal conductivity of the surrounding liquid, and R is the distance from the heat source. The absorption inside a trap of size w_0 is $I_{abs} = I_0(1 - e^{-w_0/\xi})$, where I_0 is the incident intensity and ξ is the absorption length of the material at the laser wavelength. We measured the absorption of a highly concentrated lipid solution (100 mg/ml DMPC in methanol-chloroform (1:1)). We found an upper bound of 0.024 on the optical density (absorbance), at 488–514 nm, from which we obtained an upper bound of 0.16 liter/mole-cm for the molar extinction coefficient, $\bar{\epsilon}$ of lipids. We consider two extreme cases in which 1) the membrane bilayer is entirely crumpled inside the trap at a concentration of $\bar{c} \approx 0.45$ mole/liter, and 2) the membrane is flat inside the trap at a concentration of $\bar{c} \approx 6 \times 10^{-3}$ mole/liter. The absorbance inside the trap of size $w_0 \approx 0.3$ μm is $w_0/\xi \equiv \bar{\epsilon}\bar{c}w_0 \approx 2 \times 10^{-6}$ for the first case and $w_0/\xi \approx 3 \times 10^{-8}$ for the latter case. Hence for an input intensity of $I_0 = 50$ mW (at the trap), the upper limit of the local temperature rise is $\Delta T \approx (I_0/\lambda w_0)(w_0/\xi) \approx 0.5$ K and 5×10^{-3} K, respectively. Both results for ΔT should be taken as overestimates and upper bounds for the actual heating. For example, we have neglected local cooling due to convection.

4. PEARLING OF CYLINDRICAL VESICLES: A DYNAMICAL INSTABILITY

"Pearling" is the peristaltic transition that a membrane tube that was stabilized by curvature elasticity undergoes when a sudden tension is applied to it. Of the many excitations and transitions that we have observed in membranes, this is the best characterized by far and has played an important role in our understanding of nonlinear dynamics in membrane structures. For one thing, it is experimentally well controlled. Second, it can be formulated as a theoretically tractable one-dimensional problem. Third, it clearly shows the generation of tension in the membrane by the laser, a tension that interacts and competes with the curvature elastic energy in a manner that lies at the heart of the action of the laser on membrane structures in general. Finally, it typifies many of the problems and aspects that arise with dynamical problems: strong coupling to the surrounding flow, universal behavior and critical exponents at the transition, dynamical selection of velocities and wavelength, strong fluctuations and their interplay with the linear growth regime, and a complex evolution of the fully developed nonlinear regime. Clearly this is a rich system, exhibiting a variety of complex phenomena, yet it is simple enough to be understood in some depth.

Beyond establishing the existence of the instability, our efforts have mainly concentrated on elucidation of the onset and linear stage. Already this proved nontrivial, because the thermal fluctuations compete with the hydrodynamic modes at onset and mask the linear stage, which we were unable to stabilize. An experimental challenge would now be to slow down or otherwise control the linear stage, to measure the linear coefficients directly. Because we were unable to do that, we measured them indirectly, through the existence of propagating front solutions. Although attempts to characterize the nonlinear stage (Bar-Ziv and Moses, 1994; Goveas et al., 1997) look promising, this is clearly a different level of difficulty.

Since we reported the instability, numerous observations have been made on the excitation of pearls in a variety of other situations, usually associated with mechanically induced tension. Specially interesting examples are the pushing of the membrane from within by a microtubule (D. Kuchnir Fygenson, private communication) and the destabilization of a tether by pulling on a bead attached to the membrane (B. Pouligny, private communication).

Schematically, the mechanisms and stages in the progression of the pearling instability can be described by the following flow chart: Laser action → Competition of tension and curvature → Instability → Flow and Dynamics → Threshold and onset → Propagation → Marginal Stability Criterion → Quantitative comparison to Linear Theory → Nonlinear regime.

4.1. Phenomenology

Our picture of the instability is as follows. The laser grabs the membrane at one point and begins pulling in lipid from the membrane that is outside of the trap. This causes a loss of area in the rest of the membrane, and an effective tension in it. The instability begins at the point of tweezing and propagates outward, at a rate that depends on the strength of

tweezing, or applied tension. Fig. 4 shows an example of a propagating, fully developed pearling instability. The linear sinusoidal perturbation rapidly increases in amplitude and coarsens. This tendency continues into the highly nonlinear stage, where the amplitude has peaked, making the pearls big and almost spherical, while the diameter of the tube that connects the pearls becomes extremely small.

Interestingly, if the pearling has developed into the nonlinear stage, then after the laser is shut off we observe that pearls flow back and migrate toward the point of tweezing, where they collect until the tension relaxes. Measuring a decay of migration velocity shows that there is a monotonic decrease in the tension after the laser is turned off.

A striking aspect of the instability, which differentiates it from other phenomena in membranes, is the nonlocal effect of the localized laser action. Nowhere else does a force, caused by the focusing of light down to a 0.3-μm spot, cause the instability of a membrane structure for hundreds of microns. This proves the global nature of the pearling instability, and dispels any worries about heating effects of the laser. This global instability is instead related to the classic Rayleigh instability of a cylinder under surface tension. An extreme example of this is given in Fig. 5 *a*, where tubes that formed junctions with each other are seen to destabilize along all of the different arms, and the pearling "jumps" across intersections (Fig. 5 *b*). Further evidence for the long range of the tension effect is seen in Fig. 6, where a collage is made of many adjacent video frames that cover a length of tube much larger than what we usually viewed.

It is possible to induce pearling by mechanical tension instead of the laser-induced tension, a fact that further strengthens our picture of the laser action. This was done by simple micromanipulation. We inserted a glass microneedle into the sample and pulled on a lipid globule that had tubes attached to it. A rapid enough pull caused elongation of the tubes and produced uniform pearling modes with both linear, small-amplitude modulations and nonlinear, isolated pearl structures. This is shown in Fig. 7, where the glass

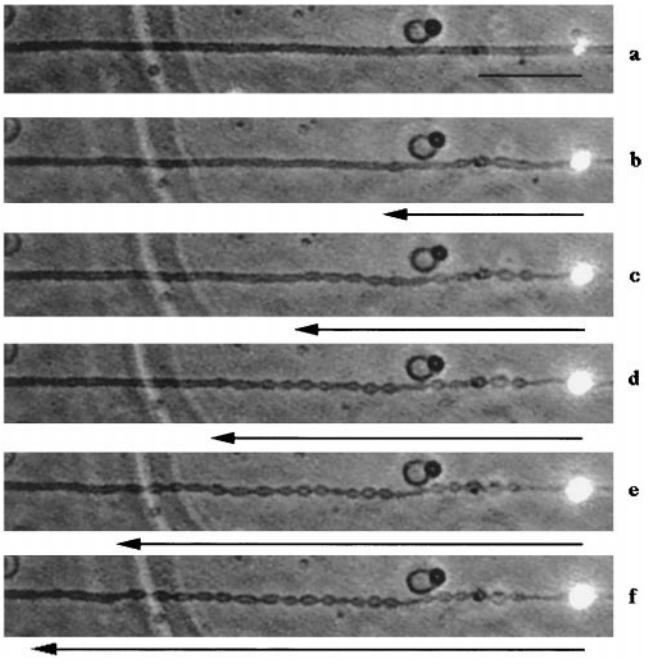

FIGURE 4 Propagation of a fully developed, large-amplitude pearling front outward from the illuminated laser spot. Time between frames in seconds: (*a*) 0, (*b*) 0.44, (*c*) 0.6, (*d*) 0.84, (*e*) 1.08, (*f*) 1.14. The bar represents 10 μm.

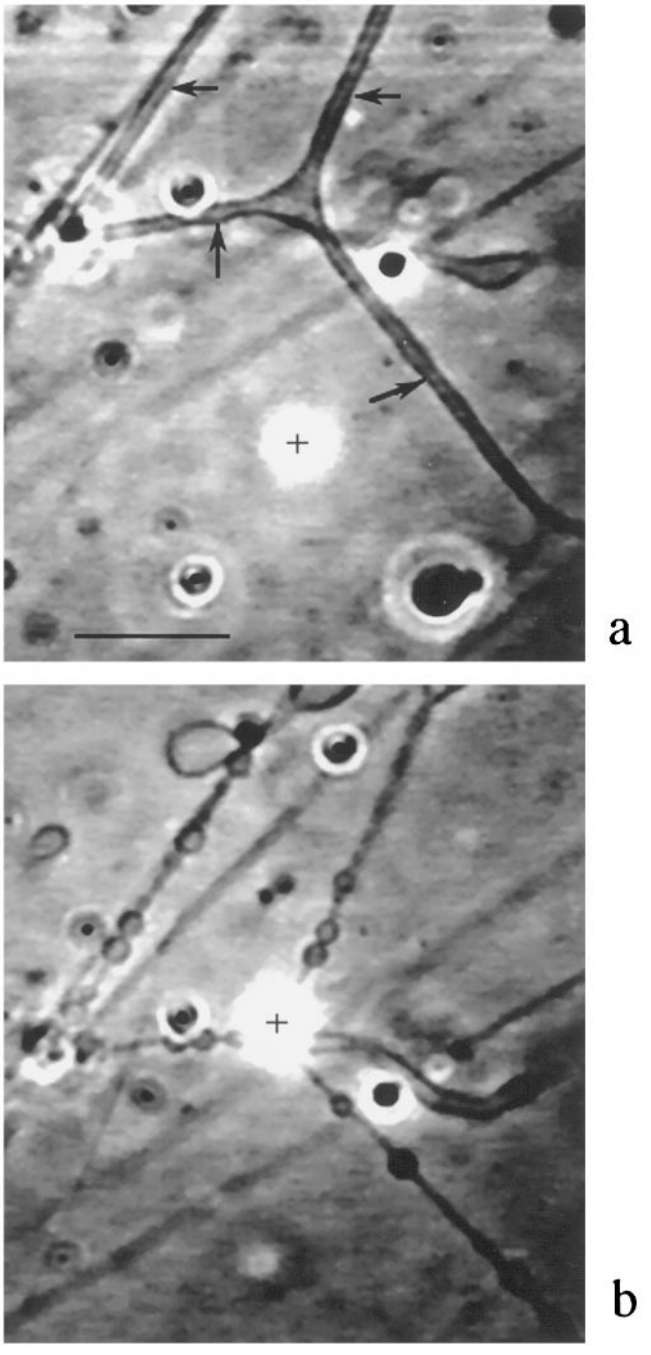

FIGURE 5 (*a*) A network of connected intersecting tubes made from DGDG lipids. The marks indicate different sections of the tube, and the crosses indicate the position of the laser tweezers. (*b*) Upon tweezing of the tube at one place, the instability propagates to all sections. The tube here has reached the nonlinear stage, and the pearls are stable over a long time. The bar represents 10 μm.

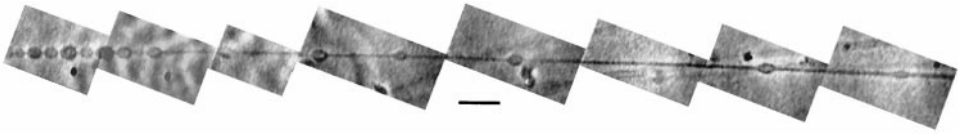

FIGURE 6 A collage of video frames showing the long range of the instability. The tweezing point was just to the left of the picture. The bar scale is 10 μm.

microneedle (not shown) was pulling at the end of the tube. The instability initiated with uniform, small-amplitude long modes and then transformed into isolated spherical pearls connected by thin tubes, exactly as in the laser induced case. An additional example is presented in Fig. 8, where we induced pearling by using the tweezers to drag a bead that was encapsulated in the vesicle wall.

Because a globule is an infinite reservoir of lipids, one can, in principle, mechanically draw tubes of increasing length without inducing tension (and hence pearling) by pulling slowly, so that new lipid can flow along with the pull from the lipid reservoir. However, if the pull is rapid and the tube long enough, lipid cannot flow from the globule, and the surface area of the tube is effectively fixed. For the tweezers, no lipid is added near the trap. Thus membrane can only be delivered by a transformation to a new shape of equal volume but less area per unit length.

The production of tubes and their subsequent robustness are in themselves an interesting issue. Our tubes are all metastable, ending up after many hours (about a day) as a large sphere on a very thin tube. The fact that these tubes come in a range of radii and lengths, and that they still evolve as we observe them, complicates the picture sufficiently that at present there is no explanation of the exact details of their production and evolution.

4.2. Overview of theoretical approach

4.2.1. Basic considerations and assumptions

The origin of the pearling instability of a membrane cylinder can be understood as a competition between the curva-

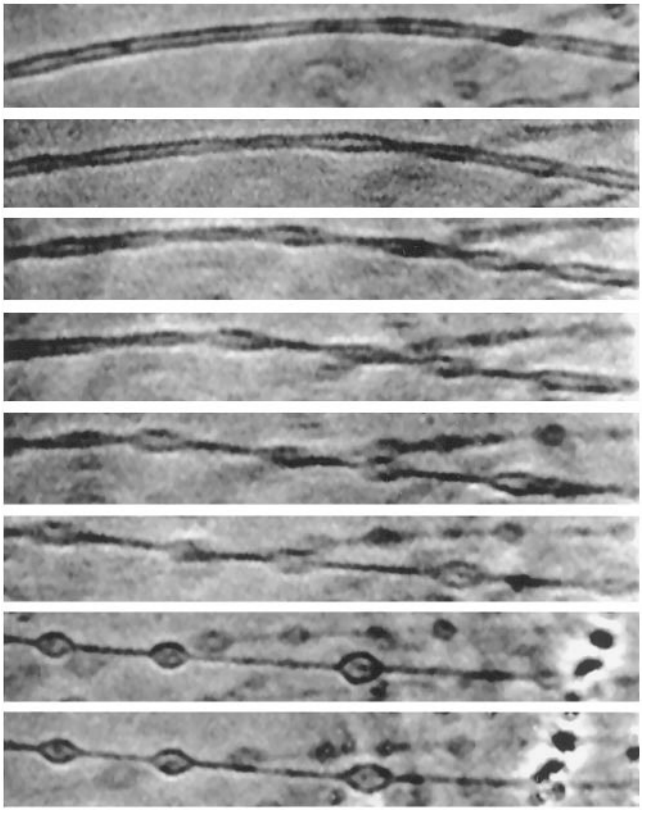

FIGURE 7 Pearling by a rapid mechanical pull with a glass microneedle. The needle (not shown, on right side of frame) was positioned perpendicular to the tube axis, and the direction of the pull was parallel to the axis.

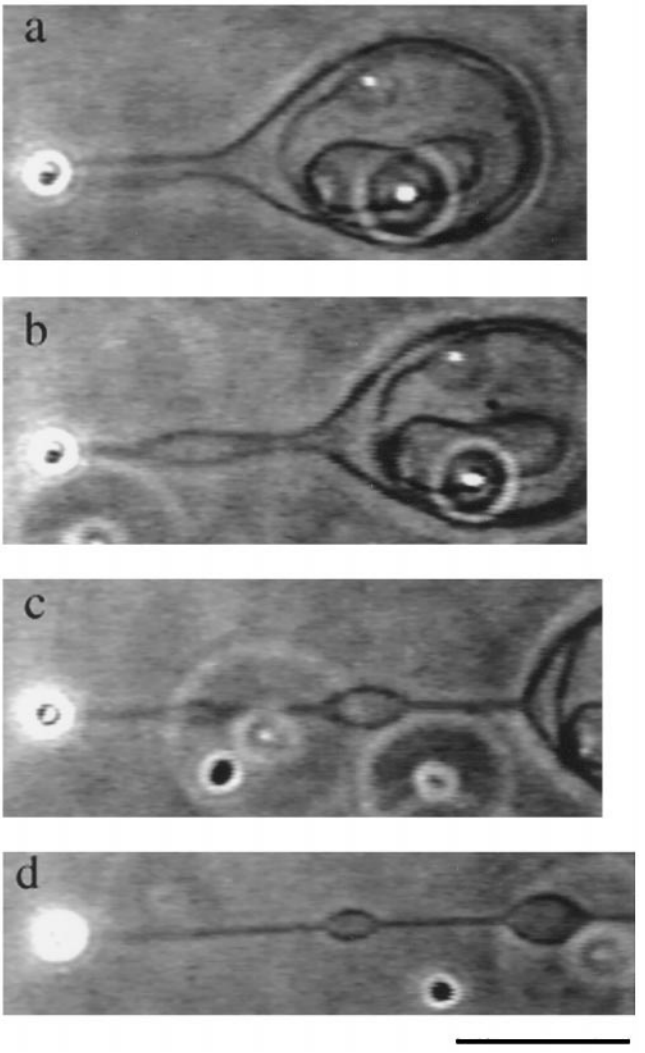

FIGURE 8 Pearling by several rapid mechanical pulls performed consecutively on a silica bead that was encapsulated in a vesicle and trapped by the tweezers. The typical time scale is seconds, and the tugging velocity was typically 15 μm/s. The bar represents 10 μm.

ture elasticity that stabilizes the tube and an externally applied surface tension that destabilizes the tube (Bar-Ziv and Moses, 1994). As mentioned in Section 2.3 the destabilizing effect of tension arises from the geometrical fact that long-wavelength deformations on a cylinder can reduce the surface area while maintaining its enclosed volume, thus satisfying the tendency of a positive surface tension to minimize area. The most simplified approach is to assume that the tension is constant in time and uniform along the tube. In Section 2.3 we recalled the argument of Goldstein et al. (1996) that the laser applies a sudden tension that spreads rapidly along the tube due to the incompressibility of the membrane. Thus tension exists in the membrane before any shape transformation can occur, and one can analyze the initiation of the instability, assuming a constant tension. The same argument holds for the mechanically induced instability where, by applying a rapid pull on a globule with an attached tube, we induce a sudden force per unit length (tension) along the tube before a change of shape can occur.

Granek and Olami (1995) have proposed an alternative time dependence of the laser-induced tension resulting from two competing effects: an assumed constant suction rate of surface area, rather than the constant tension assumed here, and the stabilizing tendency of the membrane to revert to zero tension. Their analysis predicted a coupling between the time-dependent surface tension and the growth of the instability. We have not been able to address the time dependence of the tension in our experiment and have therefore assumed constant and uniform tension, at least in the initial growth of the instability.

Olmsted and MacKintosh (1997) have argued that gradients of tension are created in the laser experiment, because at the far ends of the cylinder the membrane is attached to a lipid reservoir at zero tension. However, our field of view in the microscope limits our observation to a few wavelengths on each side of the tweezing site, which is typically chosen to be quite far from the ends of the tube, and hence we are insensitive to gradients.

4.2.2. Linear stability analysis

Consider a membrane tube subject to uniform and constant tension. The energy of the membrane is then a sum of the curvature elasticity and a surface energy,

$$F = \kappa \int 2H^2 \mathrm{d}S + \Sigma \int \mathrm{d}S. \tag{15}$$

To identify the instability we must calculate the energy of small deformations of the shape and find those modes that reduce the energy of the unperturbed tube (Bar-Ziv and Moses, 1994; Nelson et al., 1995; Granek and Olami, 1995; Gurin et al., 1996). We limit ourselves to shape deformations that are axisymmetrical and in which the axis is unperturbed (peristaltic modes). For a surface given in terms of the local radius, $R(z)$, in cylindrical coordinates the area element is $\mathrm{d}S = 2\pi R(z)\sqrt{1 + R_z(z)^2}\mathrm{d}z$, where the subscript denotes the partial derivative, and the mean curvature H is

$$H = \frac{RR_{zz} - 1 - R_z^2}{2R(1 + R_z^2)^{3/2}}. \tag{16}$$

Linear stability analysis permits us to restrict our attention to sinusoidal perturbations of the form

$$R(z) = \rho_0 + u_q \sin(qz). \tag{17}$$

The unperturbed tube radius, R_0, is related to the amplitude ρ_0 via the volume conservation constraint: $\rho_0 = R_0\sqrt{1 - u_q^2/2R_0^2}$. Integrating and keeping terms to quadratic order in u_q, we obtain the excess energy per unit length over the unperturbed tube,

$$f = \frac{1}{2}\frac{\pi\kappa}{R_0^3}\sum_k \left(\left(\frac{3}{2} - \sigma\right) + (\sigma - 1)k^2 + k^4\right)u_k^2, \tag{18}$$

where the nondimensional wavenumber is $k = qR_0$, and $\sigma \equiv \Sigma R_0^2/\kappa$ is the normalized ratio of surface tension to curvature. For $\Sigma = 0$ all wavenumbers are stabilized by the curvature. For $\kappa = 0$ we have the Rayleigh instability of a cylinder of fluid, where all modes with $k < 1$ are unstable, as they reduce the surface area at constant volume (Rayleigh, 1892). For finite Σ and κ, long-wavelength modes become unstable only above a critical value,

$$\Sigma_{\mathrm{pearl}} = \frac{3\kappa}{2R_0^2}. \tag{19}$$

4.2.3. Dispersion relation

The linear stability analysis identifies the instability control parameter and the unstable modes; it also seems to predict that, for any Σ, the most unstable mode is $k = 0$, because that is where Eq. 18 is as negative as possible. Indeed, Rayleigh's original analysis of the instability of a viscous thread gave this conclusion, leading to an irregular breakup of the thread (Rayleigh, 1892). But the pearling instability selects a well-defined, nonzero wavenumber (Fig. 4). To understand this discrepancy, note that Eq. 18 says nothing about the *rate* of growth of a mode. In fact, modes with $k \approx 0$ involve large-scale fluid motion, a process that incurs strong hydrodynamic dissipation. To obtain the growth rates of the unstable modes and the fastest growing mode, one has to solve the hydrodynamic equations of the fluid motion, which balance the tension against the viscous dissipation under the appropriate boundary conditions.

We can easily carry out these steps using a rough approximation to the hydrodynamics. Neglecting the bending stiffness for the moment, Eq. 18 reduces to an energy for mode k whose time derivative is $P_{\mathrm{laser}} = (\pi\Sigma/R_0)(-1 + k^2)u_k\dot{u}_k$. This is minus the rate at which energy is given to the system by the laser. To see where this energy goes, we note that in time δt a volume $\delta V \approx (2\pi R_0/2k) \cdot (2\pi R_0) \cdot (\delta u/2)$ of fluid needs to be moved from the narrowing parts of the tube to

the thickening parts. To do this while maintaining no-slip boundary conditions at the wall of the tube requires a central fluid velocity of $v(0) = 2\pi\dot{u}/k$, by the Poiseuille formula. The squared shear rate of this flow, times the viscosity η of water, is the rate of viscous energy loss per unit volume. Equating the total loss $\eta(16\pi^3/5k^2)\dot{u}^2R_0$ to $-P_{\text{laser}}$ then gives the approximate growth rate, $\omega(k) \equiv \dot{u}/u = (5\Sigma/16\pi^2R_0^2)k^2(1 - k^2)$. Thus we see that the growth rate indeed is not a maximum at $k = 0$, but rather at $k = 1/\sqrt{2} \approx 0.7$, roughly as observed.

Although the above derivation is transparent, quantitative comparison to the experiment requires a more accurate treatment (Goldstein et al., 1996; Bar-Ziv et al., 1997b). In particular, by neglecting bending stiffness we have missed the threshold phenomenon mentioned in the previous subsection. A useful approximate form for the complete dispersion relation is (Bar-Ziv et al., 1997b)

$$\omega(k) = \tau_\kappa^{-1} bk^2 \left[\frac{3}{2}\left(\frac{\Sigma - \Sigma_{\text{pearl}}}{\Sigma_{\text{pearl}}} \right)(1 - k^2) - k^2 - k^4 \right], \quad (20)$$

where $b \approx 0.04$ and $\tau_\kappa = \eta R_0^3/\kappa$. The k^2 multiplier is familiar from the simplified treatment in the preceding paragraph; it reflects the dissipation of long modes. The terms in the brackets originate from the curvature and surface energies of the mode. The dispersion relation predicts a continuous transition with a selected wavenumber of $k_{\max} \approx 0$ at onset and $k_{\max} \to 0.68$ for larger values of the control parameter (Goldstein et al., 1996).

4.2.4. Marginal stability criterion and linear response

Most theoretical work to date has focused on the initial, linear instability (but see Goveas et al., 1997). This represents a major obstacle to quantitative comparison of theory and experiment, because the linear stage cannot be stabilized experimentally, nor can its growth rate be measured directly. In fact, the linear stage appears to be completely masked by fluctuations of the membrane, with amplitude and wavelength similar to those of the instability. We are thus driven to try to use linear theory to describe nonlinear phenomena, and this is made possible by the existence of propagation of the instability outward from the point of tweezing, in both directions along the tube. It is well known that for a variety of nonlinear systems in which a stable, patterned state (in our case the pearls) invades an unstable, uniform one (the straight, tense tube), the selected velocity and wavelength can be found from the linear dispersion relation, using the "marginal stability criterion" (MSC) (Dee and Langer, 1983; Fineberg and Steinberg, 1987; van Saarloos, 1988). This works because the front at its leading edge has small amplitude and obeys the linearized equation of motion. Using the MSC, numerical evidence has been given for the existence of a front, along with precise analytic predictions for the critical velocity and wavelength for tension Σ well above the threshold Σ_{pearl} (Goldstein et al., 1996). One surprising feature of the analysis is that the selected wavelength is slightly different from the most unstable mode, leading to a deviation from the simplified model we sketched in Section 4.2.3; specifically, the velocity of propagation was found to scale as

$$\bar{v} \equiv V/V_\kappa = 0.082\Sigma/\Sigma_{\text{pearl}}, \quad (21)$$

where $V_\kappa = \kappa/\eta R_0^2$. Close to threshold, one must solve the equations of Goldstein et al. (1996) numerically (T. R. Powers, unpublished calculation). A convenient interpolating formula approximately reproducing the solution is

$$\bar{v} \equiv V/V_\kappa = 0.082(\Sigma/\Sigma_{\text{pearl}} + 0.067) - 3713e^{-10.655\Sigma/\Sigma_{\text{pearl}}}. \quad (22)$$

Equation 22 is approximately valid for any $\Sigma > \Sigma_{\text{pearl}}$.

A different approach to analyzing the propagation is to use a linear response to calculate the response of an unstable system to a localized, point-like perturbation (Gurin et al., 1996). Because of dispersion, the perturbation diffuses from the origin and is amplified by the unstable modes. This analysis predicts an identical scaling of velocity and introduces an experimentally measurable delay time that is the typical time needed for an appreciable amplitude to develop,

$$\Delta t = 33C\tau_\kappa \left(\frac{\Sigma_{\text{pearl}}}{\Sigma - \Sigma_{\text{pearl}}} \right), \quad (23)$$

where C is an experimental parameter measuring the amplification that is needed to bring the amplitude to an experimentally measurable value (Bar-Ziv et al., 1997b).

4.3. Onset and propagation

We have recently reported a quantitative study of the onset of the instability and the propagation of unstable fronts (Bar-Ziv et al., 1997b). The experiment was carried out on tubes made from SOPC. Tubes were produced by first depositing lipid on the bottom plate, closing the cell with a top plate, and then filling the cell with water through small fill holes in the side, which were then sealed with epoxy. As the lipid structures were self-assembling, a flow was induced by gentle rubbing along the top plate of the sample cell. Lipid globules detached as a result of the flow, and the tether they left behind usually evolved into a single-bilayer tube. We determined that it was a single bilayer by optical contrast and by tweezing, which easily separated tubes that were composed of many bilayers into the separate constituent bilayers. In this specific sample the tube diameters were relatively monodisperse, almost all of them in the 1-μm range. This is probably related to the uniformity of the drag force induced by a large-scale flow. The concept of area loss by application of the tweezers was vividly exemplified on occasion by the formation of a small vesicle that was created inside the tubes upon prolonged tweezing. This vesicle typically had a radius comparable to that of the tube and was visible, differing from the fragments that we hypothesize to form an osmotic gas. Such cases were discarded in the analysis of propagation.

Experimentally, the onset of pearling occurred when the laser intensity exceeded a critical intensity I_{pearl}, which we measured to be $I_{pearl} = (10 \pm 4)$ mW on tubes of radius $R_0 = (0.6 \pm 0.1)$ μm. Using these values, we obtain $\Sigma_L = 4.5 \times 10^{-4}$ erg/cm^2 for the laser-induced tension (Eq. 3) and $\Sigma_{pearl} = 4.2 \times 10^{-4}$ erg/cm^2 for the critical tension of pearling, with errors of up to 40% in both. The rough agreement between the two estimates of the tension is a qualitative confirmation of our simple electrodynamic model for the laser-membrane interaction.

In Bar-Ziv et al. (1997b) we used I_{pearl} measured for one tube to evaluate the control parameter $\epsilon \equiv (I - I_{pearl})/I_{pearl} = (\Sigma - \Sigma_{pearl})/\Sigma_{pearl}$ for tubes with 14 values of R_0 in the range $R_0 \approx 0.4$–1.0 μm. (We also assumed that the packing energy Σ_c was negligible. We return to this point below.) For each value of ϵ we measured the position of the front $X(t) = V \cdot (t - \Delta t)$, with $t = 0$, the time the laser was turned on, and extracted the velocity of propagation V, the delay time Δt, and the selected wavenumber qR_0. We review the results for Δt and qR_0 here for completeness (Figs. 9 and 10). In particular, Fig. 10 qualitatively supports the prediction of a continuous bifurcation with long wavelength at threshold (Bar-Ziv et al., 1997b).

The determination of the front velocity as obtained from figures such as Fig. 4 relied on our ability to distinguish between a pearled state and a "straight" fluctuating tube. The difficulty in determining the front position is visually apparent, and this is a "best case," because the amplitude in Fig. 4 is actually nonlinear, and higher than the fronts that actually were used in the analysis. The arrowheads in this figure, as well those in Figure 1 of Bar-Ziv et al. (1997b), approximate a straight line and demonstrate how a propagation speed was obtained. We found out that this was done best by eye and not by our computer algorithm. Because the trap was positioned in the center of the video field of view, we typically obtained only three or four measurements of X versus t. As a consequence, the determination of the front velocity is noisy and limited, and, in particular, we are not sensitive to slowing down of the front at large distances from the trap.

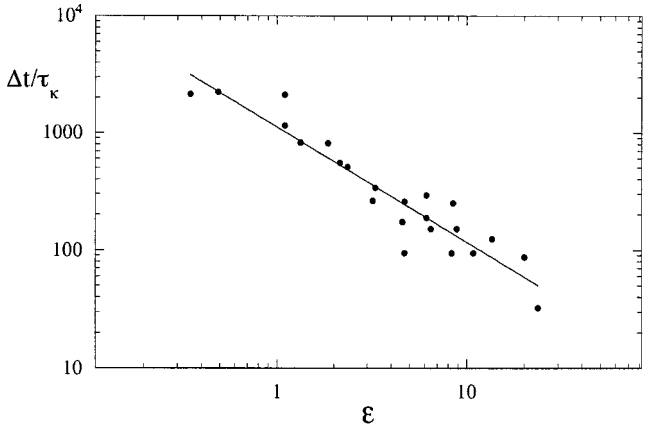

FIGURE 9 Delay time Δt scaled by $\tau = R^3\eta/\kappa$ as a function of ϵ. The best fit (*solid line*) yields $\Delta t/\tau = (1.0 \pm 0.2) \cdot 10^3 \times \epsilon^{-1.0 \pm 0.15}$. Taken from Bar-Ziv et al. (1997b).

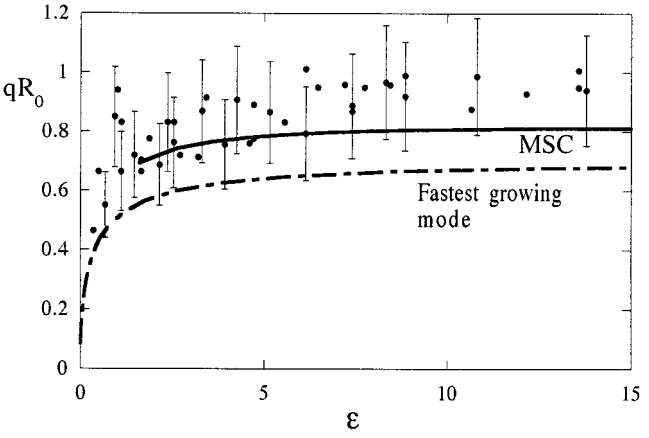

FIGURE 10 Selected wavenumber qR_0 as a function of ϵ. The theoretical predictions for the fastest growing mode from the dispersion relation of GNPS (*dashed curve*) and their MSC wavenumber correction (*solid curve*) are also plotted. Taken from Bar-Ziv et al. (1997b).

For a more detailed comparison to the MSC, we now analyze the front velocity using the interpolation formula, Eq. 22. In particular, the behavior of pearling near threshold not only tests the MSC, but also lets us say something about the possible folding energy Σ_c introduced in Section 2.4. Recall that Σ_c is a hypothetical packing cost per unit area for pulling material into the trap; if present, it reduces the effective laser-generated tension.

Rather than measuring I_{pearl} once and using it to calibrate all of the other tubes, we will now simply fit the observed front velocity $V(I, R_0)$ globally to Eq. 22 for a total of 30 trials. We take a generic form for the laser-generated tension, $\Sigma = PI - \Sigma_c$, where P is a fitting parameter. The discussion of Section 2.1 gave a rough expectation that $P \approx 5 \times 10^{-5}$ erg cm^{-2}/mW (Eq. 3), but Σ_c is unknown.

We wish to test several predictions from our theory: 1) MSC predicts constant front velocity. This is observed in every trial (data not shown). 2) MSC, combined with our dielectric model of laser action, also predicts a linear relation between velocity and laser power, as long as the latter is well above threshold. 3) Moreover, Eq. 22 claims that all of the curves $V(I)$ for various R_0 collapse onto a single universal curve when the dimensionless velocity $\bar{v}$ is plotted against Σ/Σ_{pearl}. 4) Because V_κ and Σ_{pearl} both scale as $1/R_0^2$, the slope of $V(I)$ is a universal number, independent of tubule radius. 5) As we just mentioned, we also have an estimate for the expected value of this slope.

Fig. 11 qualitatively confirms predictions 2) and 4). We carried out the fitting to P described above, again assuming $\Sigma_c = 0$. Evidently, five of the six tubule radii shown collapse onto one universal curve. We have not explained the dissident tubule; note, however, that its R_0 is not an extreme value. The data do not allow detailed assessment of 3) beyond the universality of the slope, but we note that pearling fronts do not propagate below threshold, $\sigma < 1$,

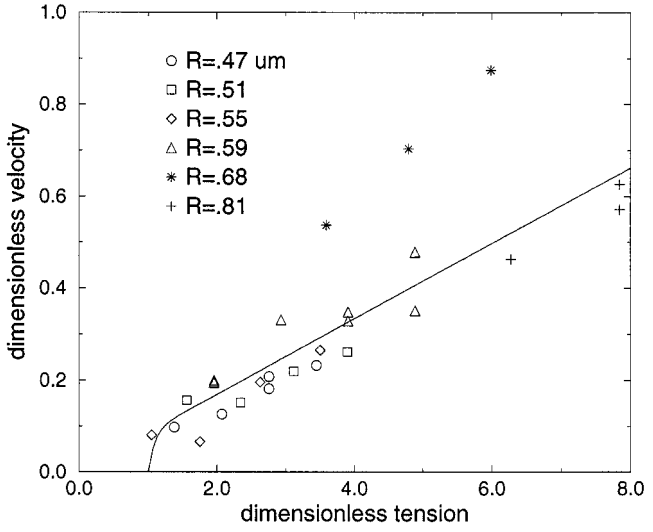

FIGURE 11 Dimensionless velocity V/V_κ of pearl propagation versus dimensionless tension Σ/Σ_{pearl} for various tubule radii R. The solid line is the theoretical prediction (Eq. 17), with Σ_c assumed equal to zero and one fitting parameter P (see text).

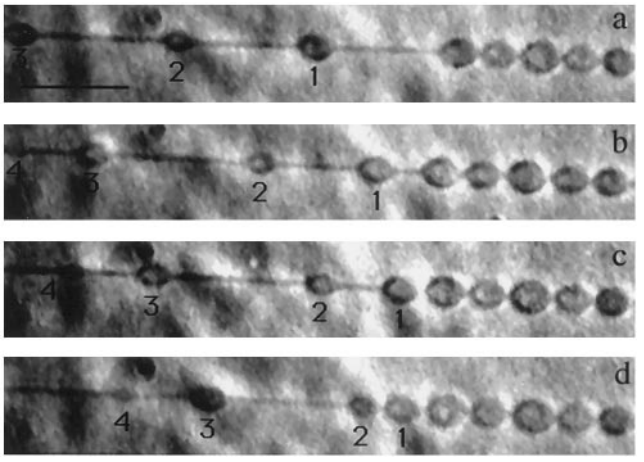

FIGURE 12 "Pearls on a string": nonlinear, late stages of an $R_0 = 1$ μm DMPC tube. The time between frames is 2 s, starting ~20 s after the laser was shut off. The bar represents 10 μm. Taken from Bar-Ziv and Moses (1994).

consistent with 3). As for 4), the fit slope $P = 2 \times 10^{-5}$ erg cm^{-2}/mW is about half our rough estimate (Eq. 3).

We were not able to extract a definite number for Σ_c, because of the scatter in the data and random and systematic errors in measuring R_0. (Note that R_0 drops out of the slope determination above.) However, we can rule out the large value naïvely estimated in Section 2.4 above, in agreement with the anecdotal evidence mentioned there. Thus the exact process taking place inside the laser spot remains a mystery. One possibility is that the dielectric forces estimated in Section 2.1 pull material into the spot, whereupon enough energy is extracted from the beam to pulverize whatever material happens to be inside.

4.4. Nonlinear stage

Longer or stronger application of the tweezers in the experiment leads to dynamic structures of isolated spheres that are interconnected by regions that have collapsed to very thin tubes (0.1–0.3-μm radius, depending on R_0). Whereas the initial instability propagates outward, these spheres travel back, flowing along the tube toward the point of application of the tweezers, where they aggregate (Fig. 12). This motion typically continues for many seconds after the laser has been turned off. The velocity of a single pearl was constant to a very good approximation over the stretch we could measure (~30 μm), ranging between 0.1 and 10 μm/s for DMPC. However, with time (measured in terms of the number of pearls, N, reaching the cluster), the velocity decreased linearly, as shown in Fig. 13. This implies a similar reduction in the force acting on the pearls. It can be shown that a linear decrease with N indicates an exponential decrease with arrival time.

The spheres are taut as they move, with all fluctuations damped by the surface tension. Eventually the pearls lose this tautness, but then they do not travel any more. The velocity of successive pearls as a function of time of arrival at the cluster is a slow relaxation decay consistent with an exponential time dependence with a time constant on the order of minutes. We did not measure the velocities as a function of the laser intensity or tweezing time.

The motion of the pearls indicates a velocity scale V_p set by a gradient of pressure along the tube $\vec{\nabla}P$. For Poiseuille flow of water in the very thin tubes that the motion of the pearls causes, $V_p = R_1^2\vec{\nabla}P/4\eta$, where R_1 is the thin tube radius. Taking as a rough estimate $\vec{\nabla}P \approx \Sigma/R_1L$, the Laplace pressure difference between pearl and tube over a typical distance L between adjacent pearls, we obtain $V_p \approx \Sigma R_1/$

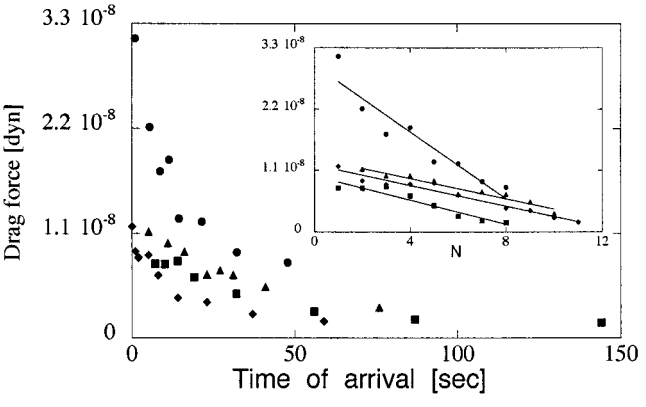

FIGURE 13 Measured velocities of successive pearls as they arrive at the cluster where the tweezers were applied. The velocities are normalized to give the Stokes drag force that they encounter, $F = 6\pi\eta Rv$, where η is the fluid viscosity, R is the pearl radius, and v is the velocity. The forces are plotted as a function of both the time of arrival at the cluster and the pearl ordinal (*inset*). Full circles designate data of DGDG, and the other points correspond to three different tubes of DMPC.

$4\eta L$. For $R_1 = 0.2\ \mu$m, $L = 10\ \mu$m, and $\Sigma = 10^{-3}$ erg/cm^2, V_p is on the order of 5 μm/s, in reasonable agreement with the measured velocities.

At this point, our experimental precision and control for the nonlinear regimen are far below what we can reach in the linear stage. For this reason, we cannot compare our results quantitatively to the theoretical predictions of Goveas et al. (1997). However, they did find qualitative agreement with some of our results. Their predicted values for the drift velocity of the pearls are on the same order of magnitude as the measured ones depicted in Fig. 13.

We conclude the discussion on cylindrical instabilities by presenting a nonstandard case, in which the axial symmetry is not conserved. This instability was observed without any laser action, but is a rare occurrence. The lowest such mode (Gurin et al., 1996) is an undulation of the cylinder. Fig. 14 shows just such an excitation, probably produced by the sudden motion of one of the globules anchoring the tube. This would lead to excess area in the tube while conserving volume.

To the best of our knowledge, there has been no previous report of an undulation with a well-defined wavelength in a fluid membrane tube. To see how this is possible, we sketch a crude model. Excess area gives rise to a negative surface tension $-\Sigma$. Assuming, as in the pearling instability, that this tension is effectively uniform, we can write the energy gained per unit length by the tube when its axis wanders as $\Sigma\delta A/L$. If the axis wanders sinusoidally with wavelength $2\pi R_0/q$ and amplitude a, then the time derivative $\mathrm{d}/\mathrm{d}t\ \Sigma\delta A/L = (\pi q^2\Sigma/2R_0)a\dot{a}$. This energy gain, in turn, is spent on Stokes drag. For small q, we have roughly a force per unit length of $4\pi\eta$ times the velocity. Equating the corresponding energy loss to the energy gain yields a growth rate of $\dot{a}/a = q^2\Sigma/2\eta R_0$, which vanishes as $q \to 0$. Thus, perhaps surprisingly, the fastest growing mode is at a finite wavelength, as observed in Fig. 14. Because the only length scale in the problem is R_0 itself, it is not surprising that the chosen wavelength is comparable to R_0.

5. LASER-INDUCED EXPULSION IN VESICLES: AN ARTIFICIAL MACHINE ON THE MICRON SCALE

5.1. Summary

In this section we introduce the tweezers into structures with spherical topology. Two classes of transformations can be observed, each raising its own problems and exposing different physical mechanisms. Spontaneous expulsion of inner content will lead us to an understanding of tension in a compact topology, and to a conjecture regarding the effect of detached membrane fragments as an osmotic gas. Expulsion under continuous action of the tweezers will lead us to invoke the suspension of lipid particles as a mechanism for generating depletion forces, which can cause vesicles to slide and peel off each other. As a bonus, it led to the unexpected observation and measurement of the "buckling" instability of a spherical vesicle in an oscillatory process that is as yet unexplained.

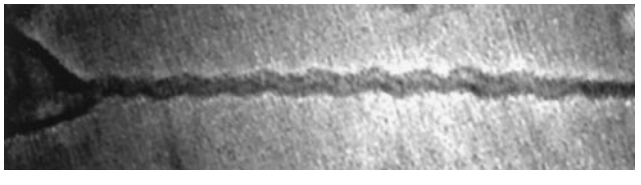

FIGURE 14 Undulation mode of a tube. This phenomenon was relatively rare, and in this case was produced in a manner unrelated to the laser tweezers. It was observed after large-scale flow in the cell.

Our preparation procedure of swelling lipids in water produces an ensemble of giant closed vesicles, which often encapsulate many daughter vesicles. These complex structures can be simplified by a continual process of tweezing in which inner vesicles are expelled, until one reaches intermediate forms of one mother–one daughter configurations. However, one often encounters such configurations without laser manipulation. Spontaneously formed and manually manipulated configurations display identical expulsion processes.

For vesicles of closed spherical topology, the action of laser tweezers induces the expulsion of interior objects from a vesicle without observable damage to either the "parent" or the "daughter" object. This phenomenon is thus quite different from exocytosis or lysis, two processes in living cells. In exocytosis the interior vesicle fuses to the outer membrane wall, opens, and empties its contents outside the cell. In lysis, the outer wall bursts, releasing the inner object along with the rest of the cell content. Remarkably, in expulsion the interior object is completely unaffected and need not even be a vesicle; we have observed qualitatively the same phenomenon with glass beads. Equally remarkably, the exit pore that opens to release the inner object heals immediately without loss of the outer vesicle's contents.

The conditions set up by laser tweezers can persist long after the laser is shut off and can lead to spontaneous expulsion of interior objects. We have reported this observation and proposed a mechanism based on the laser-induced tension. Spontaneous expulsions have been observed only after the expelling vesicles have been transformed into tense spheres, as signified by the absence of visible fluctuations (Bar-Ziv et al., 1995a; Moroz et al., 1997).

Expulsion by lysis can readily be induced in bilayer vesicles by osmotic shock, by using a sugar solution that produces a sudden pressure change (D. Kuchnir Fygenson, unpublished observations). This pressure difference is hard to estimate, because the solute is released at a point distant from the vesicle, and the concentration grows in a diffusive profile that cannot be meaningfully characterized. The surprising fact about the laser expulsion is that it is slow and nondestructive; furthermore, this dramatic membrane reorganization happens for tensions estimated to be 1000 times smaller than what is normally required for rupture. Our main hypothesis in explaining spontaneous expulsion was that the laser trap pulls in lipid and ejects it in the form of

submicron objects, the osmotic pressure of which then drives the process (Moroz et al., 1997).

Expulsion can also be induced by continuous application of the tweezers: in this case one cannot decouple the mechanical state of the vesicle from the action of the laser as we did for spontaneous events. Surprisingly, in this case the outer vesicle is not tense, so osmotic pressure alone cannot be driving the process. Whereas spontaneous expulsion takes place typically within a fraction of a second, events in which the laser acts continuously can take up to a few minutes, during which there is a constant feedback between the state of the membranes and the constant influx of energy coming from the laser. We will describe in Section 5.2 below a single experiment in which an initially complex vesicular structure was simplified in two steps, during which the laser was acting continuously. Thus far we have observed this exact process of events only once, so we cannot present a detailed model. Instead we will propose a qualitative explanation below.

In the first part of this section we review our results on spontaneous expulsion in greater detail than in previous reports. We then present quantitative image analysis of the more complex expulsions induced by active tweezing, and discuss possible explanations.

5.2. Spontaneous expulsion

Fig. 15 shows 20 frames, 0.12 s apart, of a typical giant spontaneous expulsion event. Several questions arise concerning the energetics and dynamics of such a process: What nucleates the pore, what drives the inner vesicle out, and what maintains the process? We will argue that once the exit pore opens, the process is driven by the osmotic activity of a colloid of submicron lipid fragments created by the laser, and the corresponding Laplace surface tension. We will describe the stages leading to expulsion, elaborate on new measurements, and review the model that has recently been proposed.

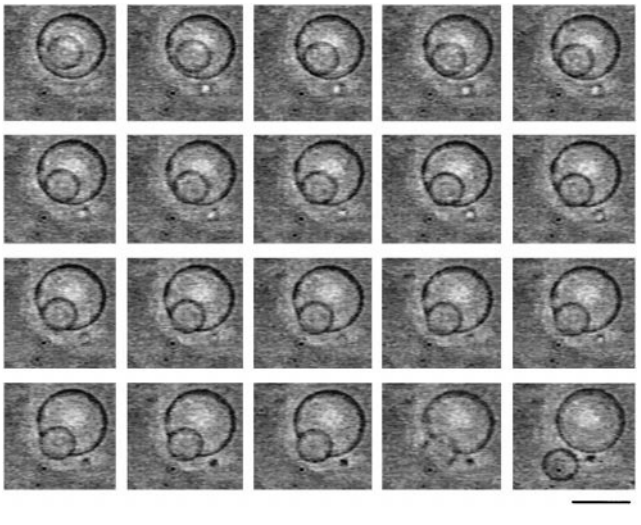

FIGURE 15 Spontaneous expulsion after laser tweezing. Concentric vesicles (SOPC) were produced spontaneously, often with multiple daughters. Both mother and daughter were initially in a floppy state, which had to be tweezed before arriving at the state shown at top left. Frames are 0.12 s apart. The bar represents 10 μm. Time progresses from left to right and from top to bottom.

5.2.1. Laser-induced rounding

Our experiments so far have indicated that spontaneous expulsion occurs only after the parent vesicle has been converted into a spherical shape. The typical effect of the tweezers on an initially flaccid vesicle is shown in Fig. 16. Characteristic shape fluctuations of a floppy vesicle are shown in Fig. 16, *a–c*. The laser tweezers were then applied to the vesicle (Fig. 16, *d* and *e*), and during a period of ~2 min or so, the fluctuations decreased until they were no longer apparent (Fig. 16 *f*). At this point the vesicle had become spherical and quite taut, indicating that tension was present in the membrane.

To follow the increase of tension and approach to sphericity while tweezing, we extracted the contour of the vesicle during tweezing and measured the fluctuations in the normalized mean square of the radius of the vesicle (Section 3.3).

Fig. 17 is the temporal evolution of the mean square radius for the same vesicle as in Fig. 16, showing strong fluctuations of the initially ellipsoidal floppy shape, superimposed on a gradual decrease of fluctuations as the shape approached the sphere, indicating an increase in surface tension. Vesicles pressurized in this way remain tense for hours. To obtain expulsion as in Fig. 15, we tweezed both the inner and outer vesicles until they were round and taut, and then turned off the laser to let the expulsion proceed on its own. Note that after 100 s the signal is flat, an indication of the reduced noise level obtained from the averaging involved in calculating $\langle R \rangle$.

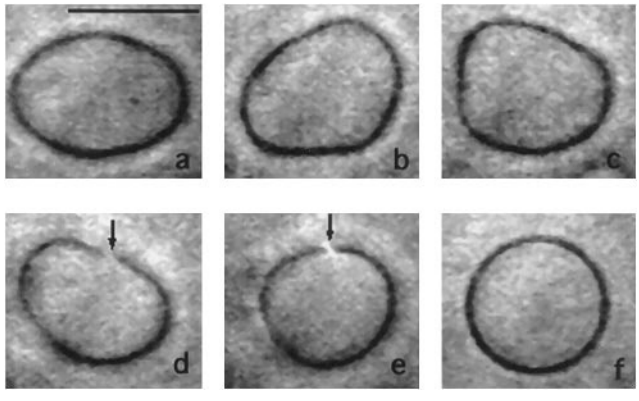

FIGURE 16 Laser-induced rounding. (*a–c*) Snapshots of the vesicle before tweezing, exhibiting typical thermal fluctuations. Tweezing (*d–e*, *arrow* marks point of tweezing) brought the vesicle to a spherical shape (*f*). The bar represents 10 μm. Taken from Bar-Ziv et al. (1995a).

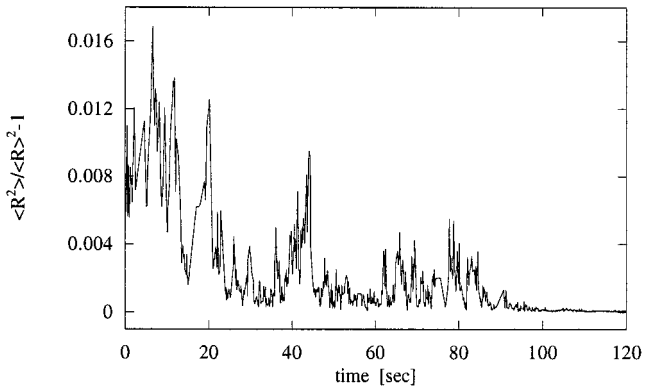

FIGURE 17 Time series of the normalized mean square of the radius of the vesicle while tweezing, reflecting the transformation of a floppy vesicle into tense sphere. Contours are 0.12 s apart.

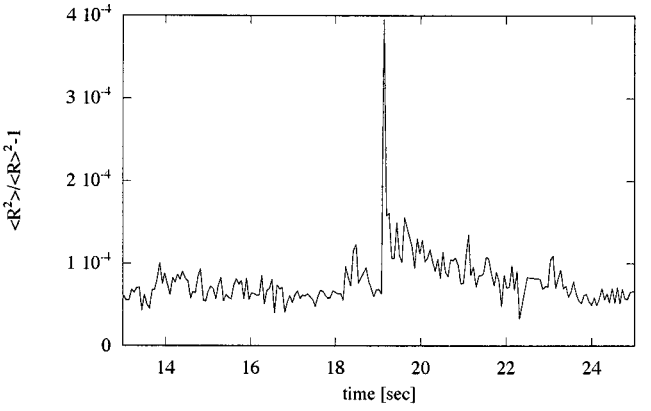

FIGURE 19 Tension-induced adhesion: normalized mean square of the external vesicle's radius during the snap to adhesion. The spike indicates the jump in the vesicle shape and is a rapid deformation, followed by a slow relaxation to the spherical shape. Data points are separated by 0.06 s. The noise level of our digitizing algorithm is reduced in this averaging process. The noise can be estimated from the fluctuations up to $t = 18$ s, because the vesicle before buckling is perfectly spherical within our resolution. We see that a perfect sphere is identified to within under a percent of the radius, or 5×10^{-5} in these nondimensional units.

5.2.2. Tension-induced adhesion and expulsion

Often the tense inner vesicle wandered for some seconds in Brownian motion before encountering the outer wall. Upon a close enough approach, adhesive forces snapped the vesicles together rapidly, sometimes visibly deforming the outer vesicle toward the inner one before the two could draw together. Fig. 18 shows snapshots of two vesicles, a few seconds after they were tweezed. In this event we did not observe expulsion. After some wandering (Fig. 18, *a* and *b*), the inner vesicle snapped into the outer one, deforming its shape (Fig. 18 *c*) and then slowly relaxed back (Fig. 18, *d–f*) while they still adhered to each other.

Indeed, a measurement of the normalized mean square of the vesicle radius shows a rapid deformation of the outer vesicle, followed by a slow relaxation of the deformed mode (Figs. 18 and 19). Going back to Fig. 15, we see that after a short waiting period the inner vesicle indeed began to emerge by first snapping to adhesion. Tension-induced adhesion of vesicles is expected to occur very close to the spherical limit (Evans, 1985; Servuss and Helfrich, 1989; Lipowsky and Seifert, 1991; Seifert, 1995b; Helfrich, 1995).

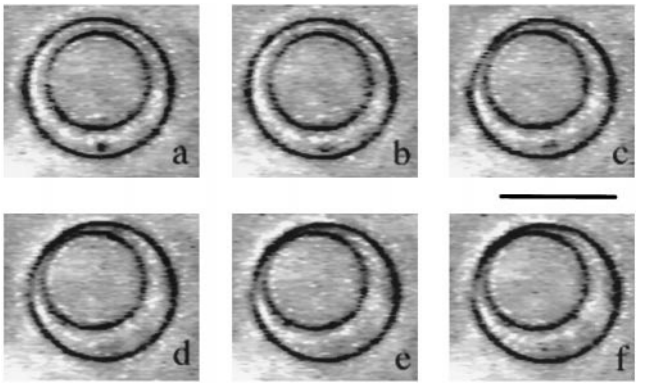

FIGURE 18 Tension-induced adhesion. Both vesicles have been laser tweezed. A strong deformation of the outer vesicle was observed (*c*) as it snapped into contact with the inner one. In *d–f* the deformation relaxed while the vesicles stayed stuck together. Frames are separated by 0.06 s. The bar scale represents 10 μm.

In general, the point of initial tweezing was not related to the point of the subsequent exit. Although the daughter vesicle's volume was sometimes as large as 40% that of the parent, the parent always remained tense through the halfway point. In most events the daughter vesicle slowed considerably near the halfway point, and in some it stalled and retracted before this. Every vesicle that passed the halfway point completed its exit rapidly, in one or two video frames.

We analyzed another giant expulsion event, similar to that in Fig. 15, and showed that the volume and area of the daughter remained roughly constant, from which we infer that at least one of its monolayer walls was intact throughout (Moroz et al., 1997). Remarkably, the area of the *outer* vesicle also remained constant through the halfway point. (Actually, we cannot measure the area or volume of a flaccid vesicle, because our method relies on knowing that the shape is spherical. What was observed is that the area is constant at least through the halfway point, because in all events the outer vesicle remained tense and spherical at least this far. For events remaining tense all the way to completion, the area-conservation law held at all times.)

Thus not only was the final surface area equal to the original, but at every intermediate step the outer vesicle area (excluding the absent cap where the daughter is emerging) remained constant. Correspondingly, the volume ΔV of the space between the vesicles was not constant, but rather grew. In the final state the outer vesicle could end up flaccid (the case of a large daughter; Moroz et al., 1997) or could remain tense (the case of smaller daughters; Fig. 15). We will present below a geometrical argument explaining when an expelling vesicle ends up flaccid and when it remains

taut. The daughter was fully detached and could be readily pulled away by the usual tweezer manipulation; there was no tether connecting it to the outer vesicle.

Others have reported expulsion from vesicles tensed with the pipette method or osmotic shock (D. Zhelev, private communication; D. Kuchnir Fygenson, private communication). Their events seem to require far greater tensions than the ones reported here. Furthermore, occasionally small vesicles with umbilical attachments can turn themselves inside out and thus appear to pass through a vesicle wall (E. Evans, private communication). We will return to this possibility below. Vesicle expulsion can also be induced by chemical means (Menger and Gabrielson, 1994). The phenomena we found are triggered solely by laser action. Finally, prompt laser-induced fusion of biological cell membranes has been reported by Schierenberg (1987); the mechanism appears to be quite different from the spontaneous rearrangement of pure lipid bilayers described here.

5.2.3. Model for spontaneous expulsion

For concreteness we will discuss the event shown in Moroz et al. (1997), in which an outer vesicle of radius $R = 4.5\ \mu$m expels an inner one of radius $r = 3.3\ \mu$m. The direct observation of membrane tension Σ implies a corresponding hydrostatic pressure $p = 2\Sigma/R$ inside the large vesicle, and yet water is clearly seen to be entering, not leaving, the intermembrane space. This is direct evidence for the osmotic flow mechanism described in Section 2.5: an excess of some solute in the interior maintains p while pulling more water in to dilute the solute (Oster and Peskin, 1992). With up to an atmosphere of osmotic pressure due to sugar on both sides of the outer vesicle, significant volume change via permeation through the bilayer is impossible. (Moreover, the known permeation rate of 70 μm/s for DMPC (Needham, 1995) is much too small to give the observed influx.) If, however, a gap of width w much larger than a sugar molecule opens, then small solutes like sugar become irrelevant. (We will return in a moment to the origin of the gap.) Indeed, performing the experiment with a wide range of sugar concentrations had little effect on expulsion. As in Section 2.5, we propose that the relevant osmotically active species is rather a suspension of membrane fragments.

For concreteness we will again illustrate our mechanism as in Section 2.5, using the smallest reasonable value for the size of these fragments, $r_{\text{colloid}} = 5$ nm. To estimate the volume fraction ϕ, we note that roughly 10% of the original 250 μm^2 of surface disappeared permanently in the initial tweezing. Following Section 2.4, we suppose that it was converted to N spheres of volume $(4\pi/3){r_{\text{colloid}}}^3$, about half of which are created outside the vesicle and escape. Because 10% of the original membrane occupied a volume of $0.1 \cdot 250\ \mu\text{m}^2 \cdot 4$ nm, we get $N/2 \approx 10^5$ trapped spheres, or a volume fraction $\phi \approx 2 \times 10^{-4}$. The ideal gas formula (van't Hoff's law) then gives an osmotic pressure $\Delta\pi \approx k_B TN/2\Delta V = 17$ dyn/cm^2.

The pressure $\Delta\pi$ and the corresponding Laplace surface tension $\Sigma = \Delta\pi R/2 \approx 4 \times 10^{-3}$ dyn/cm must overcome a line tension γ_0 to enlarge the exit pore. We can estimate γ_0 directly by studying the rapid completion stage of expulsion. Here the exit pore snaps shut, propelling the inner vesicle a few microns in one or two video frames. From the pictures we estimate a speed $v \approx 3 \times 10^{-3}$ cm/s. Setting this equal to the Stokes drag on a sphere of radius $r = 3.3$ μm gives the order-of-magnitude estimate for the line energy $\gamma_0 \approx 1.4 \times 10^{-7}$ dyn. Other events gave similar values. (Many authors have measured lipid bilayer line energies via electroporation and osmotic or hydraulic pressure in lipids different from ours (e.g., Taupin et al., 1975). Although most obtain values larger than our direct estimate, all are within a factor of 10. It is possible that a contamination or conversion of lysolipid, perhaps due to the laser itself, reduces our line tension.) As soon as the pore size exceeds $\gamma_0/\Sigma \approx 0.4\ \mu$m, the Laplace surface tension will be able to overcome the edge energy and the pore will grow.

Having identified a suitable driving force, we now turn to the actual osmotic flow. We argued earlier that a macroscopic pore must open to defeat the volume-clamping effects of dissolved small solutes, which far outnumber our hypothetical membrane fragments. This pore must also be wide enough to admit water at the observed rate Q, which is as large as 100 μm^3/s (Moroz et al., 1997), and yet small enough to trap the osmotically active species. Because the tension Σ is far too small to create significant spontaneous pores, we instead focus attention on the rim of the parent vesicle. Whereas the line energy γ_0 tries to seal this rim tightly against the exiting daughter, thermal fluctuations constantly keep it open. We can estimate the average width w of the gap by adapting Helfrich's "steric repulsion" argument (see Lipowsky, 1995). At the halfway point of expulsion, the rim of the exit pore is a tense fluctuating line, and so it feels an effective repulsive free energy of $1.89 \cdot (2\pi\tau(k_B T)^2/\gamma_0 w^2)$, pushing it away from the daughter. The line tension, however, creates a two-dimensional "disjoining pressure," or another contribution to the effective free energy of $2\pi\gamma_0 w$. Minimizing the total free energy gives an average gap width of $w = 48$ nm.

Thus the gap width w proves to be roughly of the right order of magnitude to allow free and rapid diffusion of small solutes like sugar, while still obstructing the colloidal particles and hence giving rise to the required osmotic flow. w is somewhat larger than $2r_{\text{colloid}}$, but there will still be an osmotic flow suppressed by $2r_{\text{colloid}}/w$ (Finkelstein, 1987; Moroz et al., 1997); recall also that 5 nm was just a lower bound on r_{colloid}.

We still need to estimate the rate Q of osmotic flow through a slit of width w and compare it to the experiment. For a slit of length L in a very thin membrane, dimensional analysis yields an estimate for Q of pw^2L/η, where $\eta = 0.78$ cP is the viscosity of water at 31°C, and we evaluated the geometric factor for concreteness at a pore radius of $r/\sqrt{2}$. Substituting the effective pressure $p = \Delta\pi \cdot (2r_{\text{colloid}}/w)$ and

$L = 2\pi(r/\sqrt{2})$ gives $Q \approx 14\ \mu m^3/s$, comparable to but somewhat less than what is observed.

The conserved-area rule has an interesting geometrical consequence. With it we can calculate the volume $\Delta V_{1/2}$ between two spheres at the halfway point and compare it to the volume $V_R = (4\pi/3)R^3$ of a tense full sphere with the original radius R. One finds that $\Delta V_{1/2} < V_R$ for r/R greater than $\sim 2/3$. Because the final stage of expulsion is rapid, there is no time for the required extra volume to enter, and hence the final state of the outer vesicle cannot be full. Indeed, events like the one in Moroz et al. (1997) do end up flaccid. For smaller values of r/R, the inequality is reversed: now there is no choice but to eject the excess water in a jet, and we expect the final vesicle to be tense, again as observed (see Fig. 15). There is even direct evidence for the jet: small expelled daughter vesicles sometimes end up some distance away from the parent.

Finally, we turn to the intriguing question of pore initiation. Bilayer vesicles can coexist in contact indefinitely in the absence of a specific fusogen such as Ca^{2+} ions or polyethylene glycol, or a pulse of high electric field (Chang, 1987); membranes immobilized on mica plates must be forced together with pressures of thousands of atmospheres before they spontaneously fuse (Pashley and Israelachvili, 1981). Indeed, in the absence of laser action, vesicles retain included objects indefinitely with no spontaneous expulsion; vesicle expulsion without laser action (for example, by pipette aspiration) requires tensions hundreds or thousands of times greater than those present here. What, then, creates the initial defect that nucleates expulsion?

We can rule out the formation of a defect at the laser spot, because the exit pore has no preference to form there. Instead we speculate that the same submicron membrane fragments responsible for the osmotic activity also become trapped during the rapid jump to adhesion of the two large vesicles, and then provide an alternative pathway for expulsion, circumventing the costly small-pore stage. We get a hint of how this could happen when we notice that the primary barrier to membrane fusion is the hydration force between two intact membranes. But a 5-nm fragment is hardly a smooth, intact membrane. Its enormous curvature energy of $8\pi\kappa \approx 1.5 \times 10^{-11}$ erg exceeds the line energy cost of cutting it into a flat disk, and so on average it will present large exposed hydrophobic regions. Such membrane fragments, in turn, could approach other membranes with less hydration repulsion than usual, and perhaps act as intermediaries catalyzing membrane fusion.

5.3. Expulsion by continuous tweezing: a single experiment

In this subsection we present an experiment in which new kinds of expulsions were observed. Unlike spontaneous expulsion, these transformations required continuous driving by the laser. Although this process, in its exact sequence, was seen only once, quantitative analysis of its stages reveals a surprising new phenomenon.

The initial state shown in Fig. 20 *a* consists of a tense bilayer "daughter" vesicle trapped inside a tense *double* bilayer outer vesicle. This initial three-vesicle configuration formed spontaneously in a floppy state and was pressurized by tweezing the inner and outer bilayers separately.

The experiment then consisted of two separate steps. In the first step (Fig. 21), the daughter vesicle exited from the surrounding double vesicle. This induced the formation of a new kind of "fused hole" in which the outer two "parent" vesicles locally fused to form a curved fusion neck that prevented exposure of the hydrophobic part of the bilayer. The final stage of this expulsion was characterized by a slow closure of the fused hole, allowing free volume exchange between the interior and exterior of the parent vesicles (Fig. 21 *p*). This was apparent from the gradual appearance of curvature fluctuations in the parent vesicles, in contrast to a simple pore, where rapid closure of the hole is driven by the high line tension.

In the second stage, after the daughter vesicle was fully detached and the fusion hole was closed, the two adhering vesicles were "peeled" from each other by continuous action of the laser (Fig. 22). This is a remarkable process, considering the fact that the two vesicles were of equal size! We analyzed both the inner vesicle and the outer engulfing

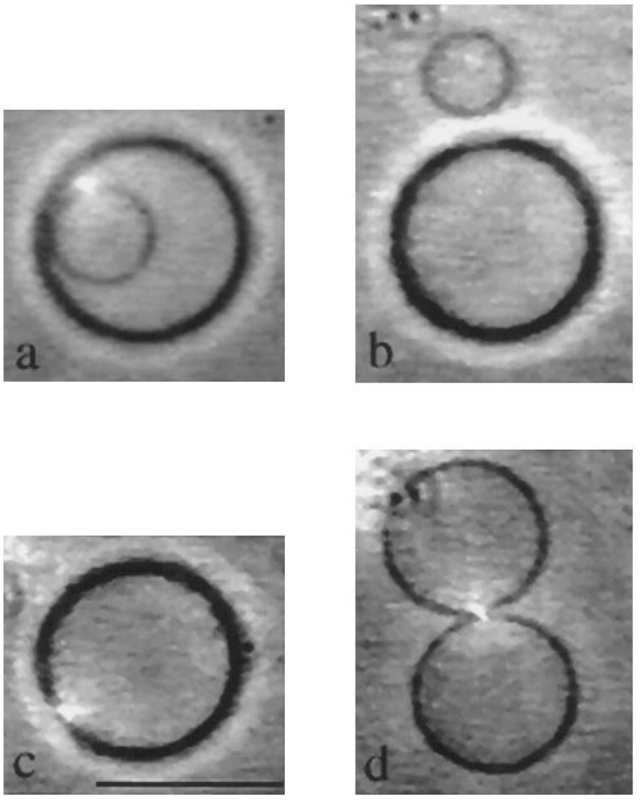

FIGURE 20 Starting points for the two steps. All three concentric vesicles were initially floppy (not shown). The tweezers were gently applied to pressurize all three and arrive at the state shown in *a*. The top row depicts the first step, starting with the daughter vesicle inside the parent vesicle (*a*). After the daughter was expelled (*b*,*c*), the two bilayers of the parent vesicle were subsequently separated (*d*). The bar represents 10 μm.

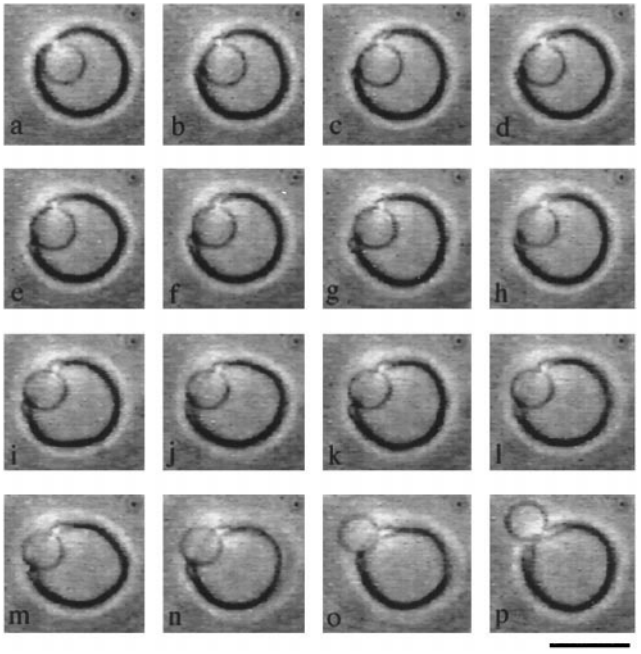

FIGURE 21 Time series of laser-assisted expulsion through two bilayers. The two engulfing vesicles fused to make a pore, marked by its curved lips, which did not close immediately after exit of the inner vesicle. Fluctuations of the outer vesicles were observed during expulsion. The frames are 1.2 s apart. The bar represents 10 μm.

vesicle and found that here, as in the first step, the outer vesicle did not remain tense during the entire process of peeling, and strong fluctuations appeared close to the final stages of the expulsion. More surprisingly, the inner vesicle exhibited a periodic sequence of buckling deformations occurring every 5 s, as the hole in the outer vesicle grew toward final expulsion (Fig. 22 *p*). The origin of the periodic shape oscillations is not entirely understood, but their observation is unexpected and gives us an opportunity to measure the buckling deformation.

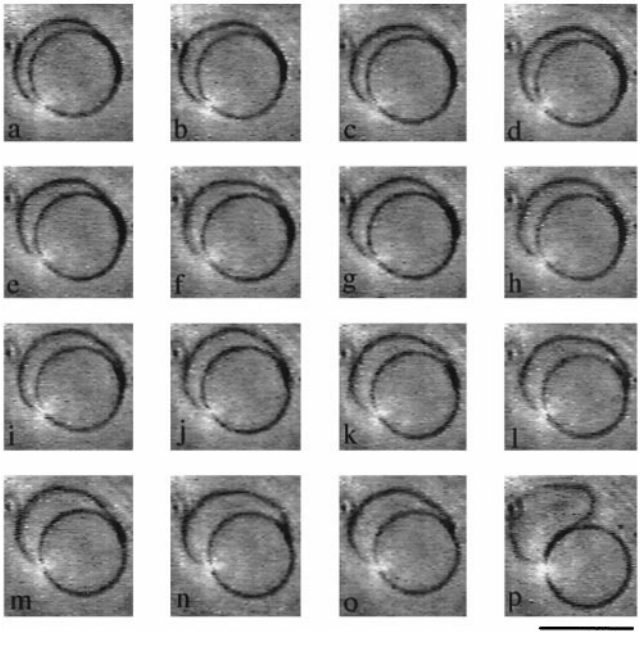

FIGURE 22 Second step: peeling a double bilayer vesicle. Video images were taken every 3 s. The bar represents 10 μm, and the bright spot is the laser trap. Time progresses from left to right and from top to bottom.

Fig. 20 shows the intermediate steps of the experiment. First, a floppy membrane and a smaller encapsulated vesicle were brought into spherical shapes by the usual action of the laser. This is the starting point of the experiment (Fig. 20 *a*). Then the tweezers clamped together the outer and inner vesicles, inducing a fusion neck between the two outer vesicles, which led to the final expulsion of the inner vesicle in a slow process described below (Fig. 20 *b*). In the second step the tweezers were focused on the two bilayers (Fig. 20 *c*) and by continuous action peeled them off (Fig. 20 *d*). The reduction of actual area by tweezing in this step is clear, because twice the area of the initial vesicle was greater than the area of the two separated final vesicles.

5.3.1. First step: expulsion through a double bilayer

Expulsion through more than one bilayer produced a new kind of defect, a "fused hole." Whereas pores in a single bilayer are elastic because of the high line energy cost of exposing the hydrophobic core of the bilayer, the fused hole must be softer, because it only involves the curvature energy. In fact, the energy of the fused pore is much lower than that of a simple pore, but the mean curvature is still greater than zero; as seen in Fig. 21, the two principal radii of curvature are $\sim$4 μm and $\sim$1 μm. Because it took the fused hole over a second to close, whereas an open pore closed within a video frame (1/25 of a second), we infer that the effective line tension γ_{eff} of the fused hole is at least an order of magnitude smaller than the line tension of an open pore. This agrees with an order of magnitude estimate of $\gamma_{\text{eff}} = \kappa/R_{\text{lip}} \approx 10^{-8}$ dyn, where R_{lip} is the radius of the connection between the two concentric vesicles. This observation in turn implies that the surface tension needed to drive expulsion can be very low, because the energy barrier for pore formation is $\Delta E \approx \gamma_{\text{eff}}{}^2/\Sigma$ (Taupin et al., 1975). This equals $\sim 10 k_{\text{B}}T$ for $\Sigma = 10^{-4}$ erg/cm^2, compared to $\sim 150 k_{\text{B}}T$ for a true pore.

The expulsion of the daughter vesicle was assisted by the laser as it pivoted around the laser spot while exiting. As stated before, and as seen in the figure, the hole did not close immediately after expulsion, but rather remained open for $\sim$2 s before retracting, implying a free exchange of fluid. The presence of thermal fluctuations during expulsion shows that the tension is low.

5.3.2. Second step: peeling and expulsion without tension

At this point we were left with a double-bilayer vesicle, which we subjected to further tweezing, with the ultimate effect of peeling the outer bilayer off, forming two separate unilamellar vesicles. This process was slow compared to

spontaneous expulsion; it lasted 60 s, during which the laser acted continuously, clamping together the vesicles at a point. As separation proceeded, the volume between the vesicles increased from nearly zero (initially, we cannot resolve the two bilayers) to a final value of about half the initial volume of the adhering vesicles. During this time the engulfing vesicle gradually slid over the inner spherical vesicle by the constant opening of a giant pore. To convey the dynamic nature of this remarkable process, we show a time series of video frames separated by 3 s (Fig. 22).

The laser point, marked by the bright spot on the left, is the place at which the pore was initiated. As peeling progressed, more area of the outer vesicle, which was initially bound to the inner spherical vesicle by adhesion, was freed by the action of the laser. Especially close to expulsion we observed the appearance of thermal fluctuations of the outer vesicle, as seen toward the end of Fig. 22.

The observation of fluctuations in Figs. 21 and 22 is a striking feature that rules out the possibility that surface tension, and hence Laplace pressure, drives the expulsion, in contrast to the situation in spontaneous expulsion (Section 5.2.3). This posed no problem in Step One, because the fused hole had a small line tension. In Step Two, however, we have a true bilayer pore. What, then, drives Step Two?

We find a possible explanation again by using our colloidal-effects framework (see Section 2.5), remembering that the laser is in operation all the while. As we noted there, the volume fraction of membrane fragments in the very small volume between bilayers can be high, leading to an energy gain per unit area of up to 0.01 erg/cm^2 when the pore creeps along the inner vesicle wall. Requiring that this gain exceed the cost $\gamma_0 2\pi \mathrm{d}(r_\mathrm{p})$ of increasing the pore size from r_p to $r_\mathrm{p} + \mathrm{d}r_\mathrm{p}$ and using the line energy $\gamma_0 = 1.6 \times 10^{-7}$ dyn estimated above, we get $0.01\ \mathrm{erg/cm^2} \cdot \mathrm{d}(\pi r_\mathrm{p}^2) \geq \gamma_0 \cdot 2\pi r_\mathrm{p}$, which is indeed satisfied when r_p exceeds 0.2 μm, a scale smaller than the laser spot size. Presumably the laser itself can disrupt the membranes to create an initial pore of this size.

Quantitative analysis of the peeling process is presented in Figs. 23 and 24. The open contour of the outer vesicle was extracted between the starting point $s = 0$, close to the laser bright spot, and the end point $s = s^*$, which we chose manually as the point where the two membranes separated on the other side of the pore. We did not take into account the area of adhesion between the two membranes, which at all times conformed to the shape of the inner vesicle. We then computed the curvature and surface integrals of the contour. The main source of high-frequency noise in these measurements is the digitization algorithm, rather than intrinsic fluctuations of the vesicle.

Looking at these two geometric quantities, we find a few striking features. The curvature integral defined in Section 3.3, $\langle(\mathrm{d}\Psi/\mathrm{d}s)^2\rangle$, remained roughly constant for most of the process. Just before expulsion it increased rapidly, as most of the membrane was no longer bound and therefore was free to fluctuate. In contrast, the surface integral $\langle\Psi^2\rangle$ did not change by much close to expulsion. Instead, it gradually

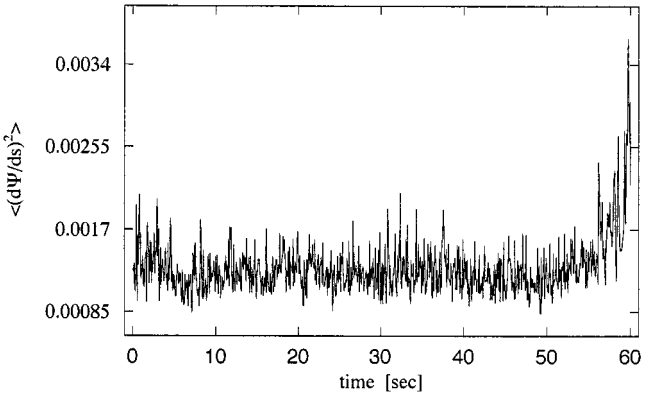

FIGURE 23 Time series of the curvature integral for the outer vesicle during Step Two (see text for detailed discussion). The time between measurements is 0.06 s.

increased from the beginning until approximately halfway through the peeling process. This measurement shows that at first, most of the energy pumped into the system by the laser was invested not only in increasing the pore size but also in unbinding the two membranes, which were held by adhesive forces. Once unbound, the area measured by our technique remains constant, and the vesicle is peeled by sliding the pore along the inner vesicle. The curvature fluctuations toward the end of the process indicate that not enough water is entering to keep the inner membrane full as its edge creeps along the inner vesicle.

5.3.3. Buckling oscillations in the second step

Another, more subtle feature observed in this peeling process is that the shape of the inner vesicle was not always spherical, but underwent sudden ellipsoidal deformations, as demonstrated in Fig. 25. As we show, these deformations displayed a periodicity of ~5 s and reflected recurrent buckling instabilities (Ou-Yang and Helfrich, 1988; Peterson, 1987). The origin of the periodicity remains obscure,

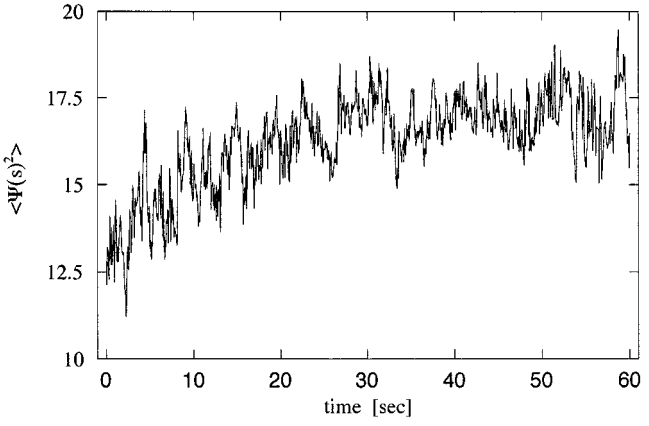

FIGURE 24 Time series of the surface integral for the outer vesicle during Step Two. The time between measurements is 0.06 s.

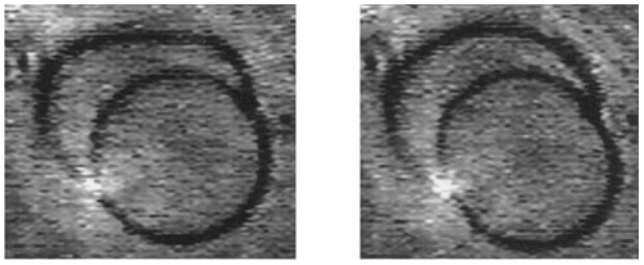

FIGURE 25 Two selected frames from the process of peeling, 0.12 s apart. In the first the vesicle is spherical, whereas in the second it has undergone a buckling instability. The outer membrane fluctuates, indicating a low surface tension.

and the opportunity to observe the dynamics of buckling cleanly and in a repetitive fashion is rare.

The buckling is most evident when we look at the ellipsoidal mode A_2 in the expansion for the vesicle contour defined by Eq. 14 in Section 3.3. Fig. 26 shows the time series of the magnitude of A_2 over the entire process of peeling for one of the half-contours of the inner vesicle.

The periodic peaks in the graph correspond to strong deformations when the vesicle buckled, and hence the shape acquired a large A_2 value. The periodicity of the oscillations is even more evident in the autocorrelation function of A_2 as defined by

$$\langle (A_2(0) - A_2(t))^2 \rangle, \tag{24}$$

which is shown in Fig. 27. The oscillations are also present in the higher mode A_3, but the signal is less pronounced and the signal-to-noise ratio is worse.

A reliable measurement of the lineshape of the buckling instability is obtained by superimposing all of the cycles of deformation, as shown in Fig. 28. This clearly shows a time asymmetry in the shape of the peak, because the vesicle buckled in ~0.1 s and then relaxed back over about a second. This is because buckling of a spherical vesicle occurs as an instability above a threshold value of external

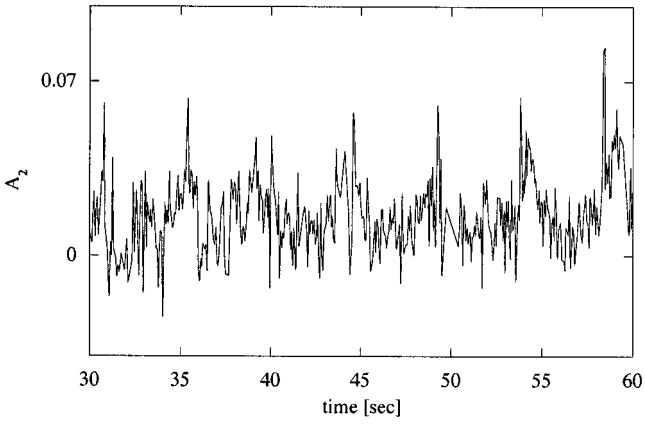

FIGURE 26 Time series of the A_2 mode of the inner vesicle during the second half of the process. The peaks correspond to buckling deformations. Data points were sampled every 0.06 s.

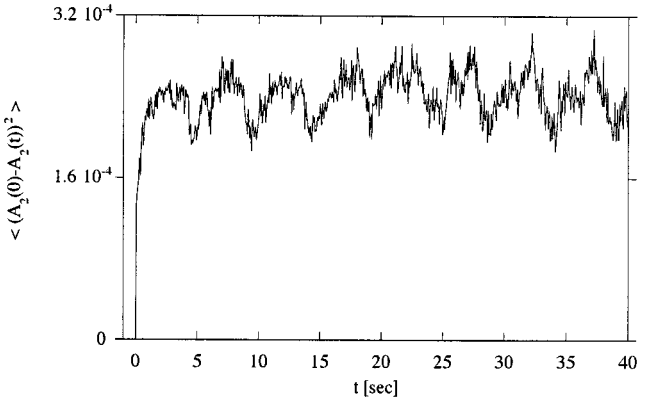

FIGURE 27 Time autocorrelation function of the ellipsoidal mode, A_2, showing the 5-s periodicity.

pressure, $P_c = -12\kappa/r_0^3$, where r_0 is the radius of the sphere (Ou-Yang and Helfrich, 1988; Peterson, 1987). This provides an estimate of the forces involved in buckling.

The origin of these buckling oscillations is not clear to us and awaits further investigation. We divide possible explanations into three general categories: 1) a local effect, such as periodic escape of the membrane from the trap; 2) a global feedback mechanism of energy storage and release, in which the vesicle buckles when the forces on it exceed a certain threshold; and 3) noise phenomena, such as mechanical vibrations.

The mechanical noise in our apparatus (Fig. 29) was monitored by looking at the flickering of the laser light reflected from the bottom plate of the cell. We selected a few square regions in the fringes produced by reflection of the optical trap from the glass bottom plate, typically five by five pixels, and measured the average intensity reflected into that region. The scattering signal has a characteristic peak around 5 Hz, typical for mechanical vibrations, but no sign of a peak at the 0.2-Hz frequency of the shape defor-

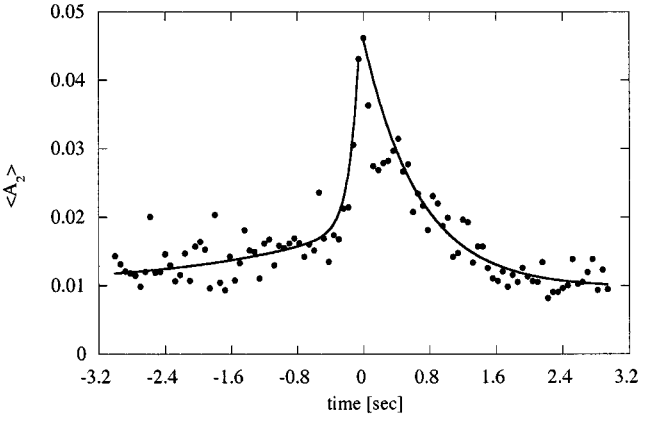

FIGURE 28 The average dynamic lineshape of the buckling instability as obtained by a superposition of all of the periodic deformations. Time $t = 0$ is the frame at which A_2 acquired a maximum value. The solid lines are each a sum of two exponential functions and guide the eye to indicate the different time scales of the excitation and the relaxation.

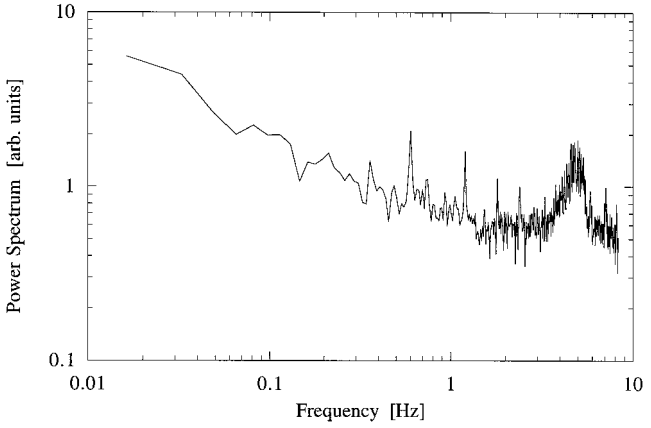

FIGURE 29 Power spectrum of mechanical noise obtained from the flickering of reflected laser tweezer light. A pronounced peak at 5 Hz is indicative of vibrations, with no indication of the 0.2-Hz buckling frequency.

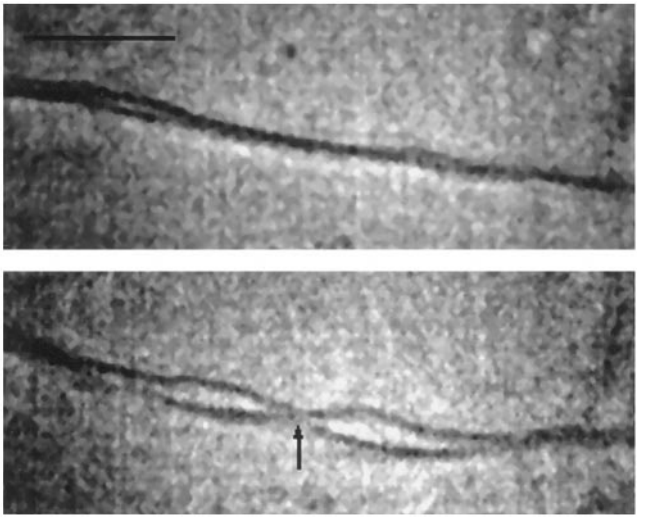

FIGURE 30 Local unbinding of pinched membranes. (*Top*) Two bound membranes. (*Bottom*) Pinching by laser tweezers (*arrow*) causes unbinding of the pair. The bar represents 10 μm. Taken from Bar-Ziv et al. (1995b), where additional details are presented.

mations. However, we cannot completely rule out other possible noise effects.

6. EXCITATIONS OF NONSPHERICAL VESICLES

6.1. Unbinding of planar membranes

Giant lamellar structures of bilayers are commonly observed after several hours of swelling, typically extending from the bottom to the top plates of the sample over hundreds of microns. These structures are mainly multilamellar and appear to be bound, or loosely bound within our optical resolution, because of kinetic constraints during formation, actual adhesion interactions, or mechanical pressure. Such bound structures have been reported in the literature (Mutz and Helfrich, 1989).

When pinching loosely bound membranes together with laser tweezers, we observed an unusual elastic response (Fig. 30). The membranes locally unbound and separated to a large intermembrane distance. One could maintain such profiles in steady state with no observable tension effects away from the trap. This is because the lateral extensions of the membranes were practically infinite.

Menes and Safran introduced a theoretical model that incorporates bending elasticity, fluctuations, and intermembrane interactions to calculate the membrane profiles subject to a local pinch, similar to a "sticker" that forces the membranes to be in close contact (Bar-Ziv et al., 1995b). This model showed that the overall binding of two membranes with localized "stickers" is strongly influenced by the elastic response and fluctuations of the embedding membrane, and is generally related to recent studies on membranes with inclusions (Dan et al., 1994). The theoretical model produced unbinding membrane profiles, which were in good quantitative agreement with the experiment, using the pinch strength as a parameter. The theory went on to predict new scaling laws for the unbinding as a function of pinch strength and size. The experiment, however, could not check these predictions because of the narrow range over which the unbinding profiles were observed by video microscopy.

A natural extension of this work could be to study the interaction of two pinches as a model for interaction between adhesion sites embedded in membranes. Although this approach has indeed been pursued theoretically (Menes and Safran, 1997), "optical pinches," produced with laser tweezers, are not the best experimental model system for the study of the response of membranes to stickers. The major drawbacks of this approach are 1) optical tweezers act continuously on the membranes, and possibly produce flow in the lipid itself and in the fluid around the pinch; 2) the packing of lipids inside the pinch is below our resolution, and we do not know the correct boundary conditions that are set at the interface of the pinch; 3) the area lost from the trap into solution could be trapped between the membranes, producing osmotic effects, as in the expulsion experiments. Thus, to model local membrane stickers one should seek a more controlled system of mechanical adhesion sites, for example, by using coated beads.

6.2. Topological passages

Membrane "passages" are cylindrical necks that connect two membranes continuously, leaving no free edges. Shapes with passages in equilibrium have been a subject of intense experimental and theoretical research, in the context of the conformal invariance of the curvature energy (Ou-Yang, 1990; Mutz and Bensimon, 1991; Julicher et al., 1993; Michalet et al., 1994; Michalet, 1994; Charitat and Fourcade, 1997). In membranous cell organelles, such as the Golgi apparatus and the endoplasmic reticulum, passages are the basic topological building blocks that partition fluid

volume by highly convoluted surfaces (Alberts et al., 1989; B. Fourcade, private communication). A passage between two concentric spherical vesicles creates a stomatocyte shape, whereas two such passages form a torus.

We show here, for the first time, how to go beyond passive observation to the active creation of such passages; instead of micromechanical means, we used laser tweezers.

Fig. 31 shows a dynamic process in which a complex passage was formed. The initial configuration was a set of four floppy planar membrane contours obtained after a few hours of swelling, each corresponding to two bound bilayers. The laser, marked by the bright spot, was focused to a spot on a pair of bilayers, pinching them together (Fig. 31 *a*). The pinch locally separated the bilayers, creating a typical unbinding profile (Fig. 31, *b* and *c*). As the overshoot grew, it reached the upper pair and fused to form a passage (Fig. 31, *e* and *f*). The laser was kept on, thereby widening the passage (Fig. 31 *g*) and forming the remarkable structure in Fig. 31 *h*. At this point the laser was moved and then shut off. The structure was not stable and decayed in two consecutive steps (Fig. 31, *i–m*).

Although it is hard to obtain three-dimensional information from these two-dimensional figures, the unstable structure of Fig. 31 *h* looks like a spherical vesicle inside a wide passage. However, it is unlikely that this is indeed a sphere, because it decayed spontaneously (Fig. 31 *i*). Upon close inspection we see that the structure of Fig. 31 *h* could be a new kind of topological excitation, which in the language of topology is a genus-2 defect. It can be envisioned as the fusion of two passages into one complex hole, with two connections from one bilayer to the other. A view from the perpendicular side would have confirmed this conjecture.

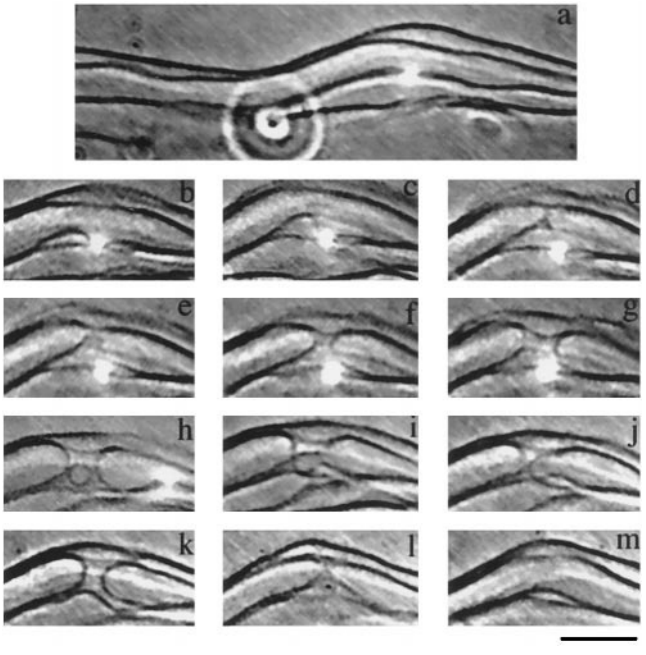

FIGURE 31 Excitation of a membrane passage with laser tweezers. (*a*) A set of four contours, each corresponding to two bilayers bound at an interbilayer distance below our separating resolution. Time of frames in seconds: (*a*) 0, (*b*) 13, (*c*) 21.5, (*d*) 22.1, (*e*) 22.6, (*f*) 22.3, (*g*) 23.8, (*h*) 26.9, (*i*) 28.4, (*j*) 29.1, (*k*) 30.6, (*l*) 45, (*m*) 71.8. The bar represents 10 μm.

6.3. Shapes with high surface-to-volume ratio

Among the variety of vesicle shapes that form spontaneously in water are those that have a high surface-to-volume ratio, such as the stomatocytes (Deuling and Helfrich, 1976). Theoretically, the shapes of vesicles are obtained as minima of the bending energy under the appropriate conservation laws and are parameterized by two physical variables, the dimensionless "reduced volume" v, and the area difference between the two monolayers comprising the bilayer, m_0 (Miao et al., 1994; Seifert, 1997). Transitions between equilibrium shapes have previously been induced by changes in temperature (Berndl et al., 1990; Käs and Sackmann, 1991). Using laser tweezers, one can excite such vesicles by rapidly "quenching" the variables v and m_0. If the laser draws an equal amount of area from both monolayers, then v must change, whereas removal of an unequal amount of lipid changes m_0. In the latter case even a small amount would suffice to excite large shape transitions. Tension is released by shape changes, because there is ample area in the vesicle to compensate for the loss and restore fluctuations.

As a result of the quench, the original stomatocyte shape is no longer the appropriate equilibrium configuration. The shape then has to dynamically relax, and we follow its trajectory in configuration space toward the equilibrium shape corresponding to the new values of the variables. Below we describe two particular examples of trajectories in configuration space during the relaxation of stomatocytes.

Fig. 32 shows an initially floppy stomatocyte vesicle. Applying the tweezers to the vesicle caused it to transform into a rimmed pancake-like shape with restored up-down symmetry. After the laser was shut off, the shape slowly oscillated between the two symmetry states of the stomatocyte configurations until it relaxed. Typically we observed one or two oscillations over a time scale of a few minutes.

The whole process of tweezing and relaxation was repeated twice for this vesicle, and on the third try the shape diverged into a completely different trajectory with no apparent symmetry. We have found no thermodynamic argument for the existence of these damped oscillations, or any dynamic mechanism that would account for them or for the long time scale.

In the second case, shown in Fig. 33, the dynamic trajectory was completely different. Another stomatocyte vesicle was chosen and tweezed. As the vesicle approached the symmetrical shape it underwent a striking bifurcation into a multifinger starfish (Wintz et al., 1996), breaking the axial symmetry. The laser was then shut off. We then observed a gradual coarsening of the shape, as the starfish lost its arms one by one.

A possible explanation (T. Tlusty, private communication) for the appearance of the starfish is the occurrence of

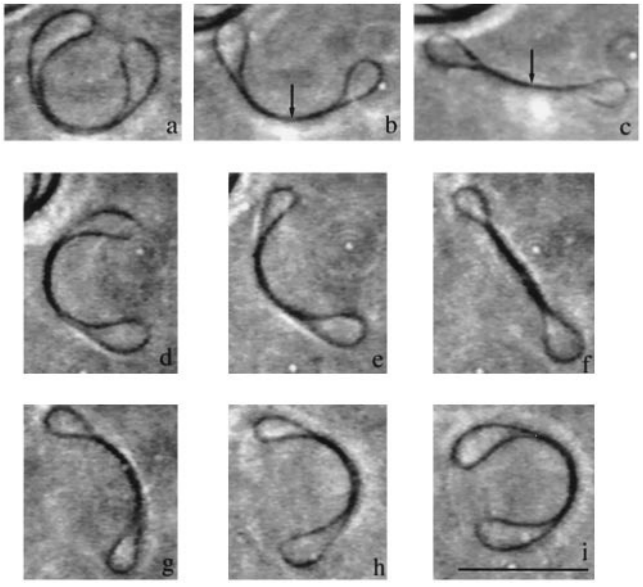

FIGURE 32 Damped oscillations of a stomatocyte. The stomatocyte of *a* was tweezed (*b*,*c*), bringing the vesicle to the symmetrical shape. The point of trapping is marked by the arrow. The tweezers were then released. The vesicle first evolved to one symmetry state of the stomatocyte (*d*), but then went back through the symmetrical state (*f*) to the opposite state (*i*). Axial symmetry is a good approximation for all of the shapes in the figure.

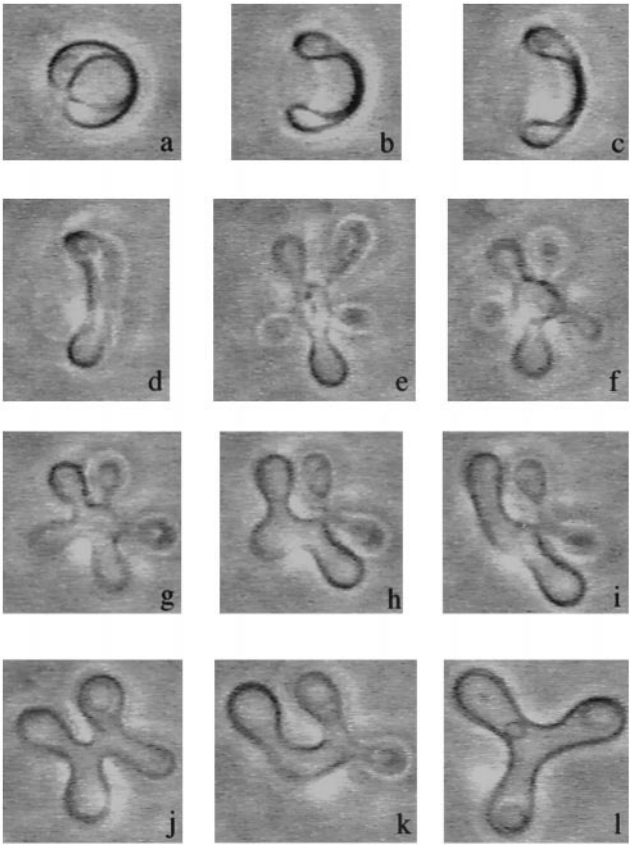

FIGURE 33 Starfish excitations. The original stomatocyte was tweezed in *a*–*c*. The bifurcation occurred between *d* and *e*. Time of frames in seconds: (*a*) 0, (*b*) 3, (*c*) 4, (*d*) 5, (*e*) 5, (*f*) 32, (*g*) 49, (*h*) 57, (*i*) 59, (*j*) 165, (*k*) 176, (*l*) 330. The laser was turned off in *c*. The vesicle continued evolving beyond the threefold starfish of *l* into a twofold shape (not shown).

a pearling instability in the rim of the stomatocyte. Assuming that the vesicle has no time to adjust its shape, tension may be built up for a short time. If at this time we regard the rim alone, it is a toroidal vesicle that can undergo pearling. One can then obtain the number of arms in the starfish as a natural consequence of the area reduction. The volume and area of the cylindrical rim are $V = 2\pi^2 r^2 R$, $S = 4\pi^2 rR$, where r is the small radius of the torus and R its big one. Ignoring the central part, a final starfish with z spherical arms and the same volume V has area $\bar{S} = (144\pi^5)^{1/3} z^{1/3} (Rr^2)^{2/3}$. To reduce area, we must comply with $\bar{S}/S \leq 1$, from which we obtain an upper limit on the number of arms $z \leq (4\pi/9)(R/r)$. Inserting $R/r \approx 4$ from Fig. 33 *c*, we get $z \leqslant 6$, in agreement with the observed shapes.

7. SUMMARY AND CONCLUSIONS

This paper combines previously unreported experimental observations with some new theoretical ideas. We have measured the optical force needed to bend a membrane, confirming the energy scale of the laser-membrane interaction. We then summarized the pearling instability and improved the analysis of the velocity scaling. We presented evidence of pearling induced by mechanical means (attaching to a bead or a micropipette and pulling on it, or by inducing a flow). A measurement of pearl migration in the nonlinear regime was presented. A first observation of a spontaneous transition to the first asymmetrical mode (undulation at finite wavelength) of a tube was presented.

The discussion of expulsion in vesicles divides into a part dealing with spontaneous expulsion after tweezing, and a part dealing with expulsion under continuous tweezing. We have quantified the steps leading to spontaneous expulsion: a measurement of the gradual decrease of fluctuations while tweezing, and a measurement of the snap to adhesion as a precursor to expulsion. In the second part we analyzed in detail the consecutive expulsion of three concentric vesicles. This uncovered phenomena such as the fused hole formed between adhering bilayers, and "buckling oscillations" as one vesicle is peeled off another. The buckling instability was quantified and its full dynamic trace measured.

We reported the first observations of mechanical excitation of topological defects, in the form of fused necks between parallel bilayers. Excitation of stomatocytes leads to relaxation via novel oscillatory behavior and to a cascade of exotic starfish configurations.

The theoretical picture we presented includes a comprehensive treatment of the folding of a membrane into the electromagnetic trap formed by the tweezers. As lipids are packed into the submicron spot they are repackaged and expelled into the solution. There they can act as an osmotically active suspension that produces and maintains a pressure as expulsion proceeds.

We have introduced the idea of colloidal creeping and have shown that it may explain some of the motion of one membrane along another, as the laser is applied.

A main hypothesis, the repackaging of lipid into subresolution membrane fragments, has no direct proof but much circumstantial evidence. This calls for possible experimental verification. The best candidate at the moment is localized dynamic light scattering (LDLS) (Bar-Ziv et al., 1997a), a technique specially developed to probe dynamics on the micron scale in a specific single region. Attempts at using fluorescence failed because of the high laser intensities.

At present we do not have a microscopic understanding of what really goes on inside the trap, but observe the resulting effect of tension outside. Still, we may have missed essential ingredients associated with chemical processes involved in the laser-membrane interaction.

The use of the laser tweezers makes possible a new approach for dynamic excitations in lipid bilayers. Ideally, this brings us closer to understanding nonequilibrium phenomena in cells and in biological membranes. The laser applies a weak tension, pulling in material and then detaching surface area. This is just enough to excite shape transformations without catastrophically disrupting the membrane.

We thank R. Bruinsma, N. Dan, J.-P. Eckmann, B. Fourcade, D. Fygenson, M. Goulian, R. Granek, S. Gruner, J. Israelachvili, R. Kamien, M. Kraus, N. Levit, A. Libchaber, R. Lipowsky, T. Lubensky, A. Meller, X. Michalet, S. Milner, D. Nelson, Z. Olami, C. Peskin, P. Sens, R. Zeitak, and D. Zhelev for innumerable discussions. It is a special pleasure to acknowledge our debt to T. Frisch, R. Goldstein, R. Menes, J. D. Moroz, T. Powers, S. Safran, U. Seifert, and T. Tlusty for collaboration on our earlier papers, to T. Tlusty for the argument relating starfish and pearling, and to T. Powers for the unpublished calculation leading to Eq. 22.

This work was supported in part by US/Israeli Binational Foundation grant 94-00190, National Science Foundation grant DMR95-07366, and the Minerva Foundation, Munich, Germany. We also thank the Aspen Center for Physics, where some of the work was done.

REFERENCES

Alberts, B., D. Bray, J. Lewis, M. Raff, K. Roberts, and J. Watson. 1989. Molecular Biology of the Cell. Garland, New York.

Ashkin, A. 1970. Acceleration and trapping of particles by radiation pressure. *Phys. Rev. Lett.* 24:156–159.

Ashkin, A. 1980. Applications of laser radiation pressure. *Science.* 210: 1081–1088.

Ashkin, A. 1997. Optical trapping and manipulation of neutral particles using lasers. *Proc. Natl. Acad. Sci. USA.* 94:4853–4860.

Ashkin, A., J. M. Dziedzic, and T. Yamane. 1987. Optical trapping and manipulation of single cells using infrared laser beams. *Nature.* 330: 769–771.

Bar-Ziv, R., T. Frisch, and E. Moses. 1995a. Entropic expulsion in vesicles. *Phys. Rev. Lett.* 75:3481–3484.

Bar-Ziv, R., A. Meller, T. Tlusty, E. Moses, J. Stavans, and S. A. Safran. 1997a. Localized dynamic light scattering: probing dynamics at the nanoscale. *Phys. Rev. Lett.* 78:154–156.

Bar-Ziv, R., R. Menes, E. Moses, and S. Safran. 1995b. Local unbinding of pinched membranes. *Phys. Rev. Lett.* 75:3356–3359.

Bar-Ziv, R., and E. Moses. 1994. Instability and "pearling" states produced in tubular membranes by competition of curvature and tension. *Phys. Rev. Lett.* 73:1392–1395.

Bar-Ziv, R., T. Tlusty, and E. Moses. 1997b. Critical dynamics in the pearling instability of membranes. *Phys. Rev. Lett.* 79:1158–1161.

Berndl, K., J. Käs, R. Lipowsky, E. Sackmann, and U. Seifert. 1990. Shape transformations of giant vesicles: extreme sensitivity to bilayer asymmetry. *Europhys. Lett.* 13:659–664.

Block, S. M. 1990. Optical tweezers: a new tool for biophysics. *In* Noninvasive Techniques in Cell Biology, Modern Review of Cell Biology, Vol. 9. J. K. Foskett and S. Grinstein, editors. Wiley-Liss, New York. 375–402.

Brochard, F., and J. F. Lennon. 1975. Frequency spectrum of the flicker phenomenon in erythrocytes. *J. Phys. (France).* 36:1035–1047.

Canham, P. B. 1970. The minimum energy of bending as a possible explanation of biconcave shape of human red blood cell. *J. Theor. Biol.* 26:61–81.

Chang, E. 1987. Pressure as a probe of vesicle fusion. *In* Cell Fusion. A. Sowers, editor. Plenum, New York. 353–364.

Charitat, T., and B. Fourcade. 1997. Lattice of passages connecting passages. *J. Phys. II (France).* 7:15–35.

Dan, N., A. Berman, P. Pincus, and S. A. Safran. 1994. Membrane-induced interactions between inclusions. *J. Phys. II (France).* 4:11713–11725.

Dee, G., and J. S. Langer. 1983. Propagating pattern selection. *Phys. Rev. Lett.* 50:383–386.

Deuling, H. J., and W. Helfrich. 1976. The curvature elasticity of fluid membranes: a catalog of vesicle shapes. *J. Phys. (France).* 37: 1335–1345.

Döbereiner, H.-G. 1995. The budding transition of phospholipid vesicles: a quantitative study via phase contrast microscopy. Ph.D. thesis. Simon Fraser University, Burnaby, BC, Canada.

Döbereiner, H.-G., E. Evans, U. Seifert, and M. Wortis. 1995. Spinodal fluctuations of budding vesicles. *Phys. Rev. Lett.* 75:3360–3363.

Duwe, H. P., J. Käs, and E. Sackmann. 1990. Bending elastic moduli of lipid bilayers: modulation by solutes. *J. Phys. (France).* 51:945–962.

Elbaum, M., D. Kuchnir Fygenson, and A. Libchaber. 1996. Buckling microtubules in vesicles. *Phys. Rev. Lett.* 76:4078–4081.

Evans, E. 1974. Bending resistance and chemically induced moments in membrane bilayers. *Biophys. J.* 14:923–931.

Evans, E. 1985. Detailed mechanics of membrane-membrane adhesion and separation. *Biophys. J.* 48:175–183.

Evans, E., and D. Needham. 1987. Physical properties of surfactant bilayer membranes: thermal transitions, elasticity, rigidity, cohesion, and colloidal interactions. *J. Chem. Phys.* 91:4219–4228.

Evans, E., and W. Rawicz. 1990. Entropy-driven tension and bending elasticity in condensed-fluid membranes. *Phys. Rev. Lett.* 64: 2094–2097.

Fineberg, J., and V. Steinberg. 1987. Vortex-front propagation in Rayleigh-Bénard flow. *Phys. Rev. Lett.* 58:1332–1335.

Finkelstein, A. 1987. Water Movement through Lipid Bilayers, Pores, and Plasma Membranes: Theory and Reality. Wiley, New York.

Goldstein, R. E., P. Nelson, T. Powers, and U. Seifert. 1996. Front propagation in the pearling instability of tubular vesicles. *J. Phys. II (France).* 6:767–796.

Goll, J., F. Carlson, Y. Barenholz, B. Litman, and T. Thompson. 1982. Photon correlation spectroscopic study of the size distribution of phospholipid vesicles. *Biophys. J.* 38:7–13.

Goll, J., and G. Stock. 1977. Determination by photon correlation spectroscopy of particle size distributions in lipid vesicle suspensions. *Biophys. J.* 19:265–273.

Goveas, J. L., S. T. Milner, and W. B. Russel. 1997. Late stages of the "pearling" instability in lipid bilayers. *J. Phys. II (France).* 9:1185–1204.

Granek, R., and Z. Olami. 1995. Dynamics of Rayleigh-like instability induced by laser tweezers in tubular vesicles of self-assembled membranes. *J. Phys. II (France).* 5:1348–1370.

Gurin, K. L., V. V. Lebedev, and A. R. Muratov. 1996. Dynamic instability of a membrane tube. *J. Exp. Theor. Phys.* 83:321–326.

Helfrich, W. 1973. Elastic properties of lipid bilayers: theory and possible experiments. *Z. Naturforsch.* C28:693–703.

Helfrich, W. 1995. Tension-induced mutual adhesion and a conjectured superstructure of lipid membranes. *In* Handbook of Biological Physics. R. Lipowsky and E. Sackmann, editors. Elsevier, Amsterdam. 691–721.

Helfrich, W., and R. Servuss. 1984. Undulations, steric interaction and cohesion of fluid membranes. *Nuovo Cimento.* 3D:137–151.

Israelachvili, J. N. 1991. Intermolecular and Surface Forces. Academic Press, San Diego.

Julicher, F., U. Seifert, and R. Lipowsky. 1993. Conformal degeneracy and conformal diffusion of vesicles. *Phys. Rev. Lett.* 71:452–455.

Käs, J., and E. Sackmann. 1991. Shape transitions and shape stability of giant phospholipid vesicles in pure induced by area-to-volume changes. *Biophys. J.* 60:825–844.

Lipowsky, R. 1991. The conformation of membranes. *Nature.* 349: 475–481.

Lipowsky, R. 1995. Generic interactions of flexible membranes. *In* Handbook of Biological Physics. R. Lipowsky and E. Sackmann, editors. Elsevier, Amsterdam. 548, 554.

Lipowsky, R., and E. Sackmann. 1995. Structure and Dynamics of Membranes. Elsevier, Amsterdam.

Lipowsky, R., and U. Seifert. 1991. Adhesion of membranes: a theoretical perspective. *Langmuir.* 7:1867–1873.

Marsh, D. 1990. CRC Handbook of Lipid Bilayers. CRC Press, Boca Raton, FL.

Menes, R., and S. A. Safran. 1997. Non-linear response of membranes to pinning sites. *Phys. Rev. E.* 56:1891–1899.

Menger, F., and K. Gabrielson. 1994. Chemically-induced birthing and foraging in vesicle systems. *J. Am. Chem. Soc.* 116:1567–1568.

Miao, L., U. Seifert, M. Wortis, and H.-G. Döbereiner. 1994. Budding transitions of fluid-bilayer vesicles. *Phys. Rev. E.* 49:5389–5407.

Michalet, X., D. Bensimon, and B. Fourcade. 1994. Fluctuating vesicles of nonspherical topology. *Phys. Rev. Lett.* 72:168–171.

Michalet, X. 1994. Thèse de doctorat de l'Université Paris VII.

Milner, S. T., and S. A. Safran. 1987. Dynamical fluctuations of droplet microemulsions and vesicles. *Phys. Rev. A.* 36:4371–4379.

Moroz, J. D., P. Nelson, R. Bar-Ziv, and E. Moses. 1997. Spontaneous expulsion of giant lipid vesicles induced by laser tweezers. *Phys. Rev. Lett.* 78:386–389.

Mutz, M., and D. Bensimon. 1991. Observation of toroidal vesicles. *Phys. Rev. A.* 43:4525–4527.

Mutz, M., and W. Helfrich. 1989. Unbinding transition of a biological model membrane. *Phys. Rev. Lett.* 62:2881–2884.

Needham, D. 1995. Cohesion and permeability of lipid bilayer membranes. *In* Permeability and Stability of Lipid Bilayers. E. Disalvo and S. Simon, editors. CRC Press, Boca Raton, FL. 69.

Nelson, P., T. Powers, and U. Seifert. 1995. Dynamical theory of the pearling instability in cylindrical vesicles. *Phys. Rev. Lett.* 74: 3384–3387.

Olmsted, P. D., and F. C. MacKintosh. 1997. Instability and front propagation in laser-tweezed lipid bilayer tubules. *J. Phys. II (France).* 7:139–156.

Oster, G., and C. Peskin. 1992. Dynamics of osmotic fluid flow. *In* Mechanics of Swelling: From Clays to Living Cells and Tissues. T. K. Karalis, editor. Springer-Verlag, Berlin. 731–742.

Ou-Yang, Z. C. 1990. Anchor ring-vesicle membranes. *Phys. Rev. A.* 41:4517–4520.

Ou-Yang, Z. C., and W. Helfrich. 1988. Instability and deformation of a spherical vesicle pressure. *Phys. Rev. Lett.* 61:1325.

Pashley, R., and J. Israelachvili. 1981. Hydration forces between mica surfaces in aqueous electrolyte solutions. *J. Colloid. Interface Sci.* 80: 153–162.

Peterson, M. 1987. Comments on: instability and deformation of a spherical vesicle pressure. *Phys. Rev. Lett.* 59:2486–2488.

Plateau, J. 1873. Statique Experimentale et Theorique des Liquides Soumis aux Seules Forces Moleculaires. Gautier-Villars, Paris.

Rayleigh. 1892. On the instability of a cylinder of viscous liquid under capillary force. *Philos. Mag.* 34:145–154.

Safran, S. 1994. Statistical Thermodynamics of Surfaces, Interfaces, and Membranes. Addison-Wesley, Reading, PA.

Schierenberg, E. 1987. Laser-induced cell fusion. *In* Cell Fusion. A. Sowers, editor. Plenum, New York. 409–418.

Schneider, M. B., J. R. Jenkins, and W. W. Webb. 1984. Thermal fluctuations of large quasispherical biomolecular phospholipid vesicles. *J. Phys. (France).* 45:1457–1472.

Seifert, U. 1995a. The concept of effective tension for fluctuating vesicles. *Z. Physik.* B97:299–309.

Seifert, U. 1995b. Self-consistent theory of bound vesicles. *Phys. Rev. Lett.* 74:5060–5063.

Seifert, U. 1997. Configurations of fluid membranes and vesicles. *Adv. Phys.* 46:12–137.

Servuss, R. M., and W. Helfrich. 1989. Mutual adhesion of lecithin membranes at ultralow tensions. *J. Phys. (France).* 50:809–827.

Simmons, R. M., J. T. Finer, S. Chu, and J. A. Spudich. 1996. Quantitative measurements of force and displacement using an optical trap. *Biophys. J.* 70:1813–1822.

Svoboda, K., and S. M. Block. 1994. Biological applications of optical forces. *Annu. Rev. Biophys. Biomol. Struct.* 23:247–285.

Taupin, C., M. Dvolaitzky, and C. Sauterey. 1975. Osmotic pressure induced pores in phospholipid vesicles. *Biochemistry.* 14:4771–4775.

van Saarloos, W. 1988. Front propagation into unstable states: marginal stability as a dynamical mechanism for velocity selection. *Phys. Rev. A.* 37:211–229.

Wintz, W., H.-G. Döbereiner, and U. Seifert. 1996. Starfish vesicles. *Europhys. Lett.* 33:403–408.